Numerical study of nucleate boiling

Diffuse interface simulations of steam bubble departures from superheated wall

Master's thesis in Applied Mechanics

ADAM JOHANSSON

DEPARTMENT OF MECHANICS AND MARITIME SCIENCES

CHALMERS UNIVERSITY OF TECHNOLOGY
Gothenburg, Sweden 2023
www.chalmers.se

Master's thesis 2023

Numerical study of nucleate boiling

Diffuse interface simulations of steam bubble departures from superheated wall

ADAM JOHANSSON

CHALMERS
UNIVERSITY OF TECHNOLOGY

Department of Mechanics and Maritime Sciences
Division of Fluid Dynamics
Chalmers University of Technology
Gothenburg, Sweden 2023

Numerical study of nucleate boiling
Diffuse interface simulations of steam bubble departures from superheated wall
ADAM JOHANSSON

Supervisor: Luca Brandt, Department of Engineering Mechanics
KTH Royal Institute of Technology

Examiner: Srdjan Sasic, Department of Mechanics and Maritime Sciences
Chalmers University of Technology

Master's Thesis 2023
Department of Mechanics and Maritime Sciences
Division of Fluid Dynamics
Chalmers University of Technology
SE-412 96 Gothenburg
Telephone +46 31 772 1000

Cover: Visualisation of the volume fraction of steam for nucleate boiling.

Typeset in LaTeX
Printed by Chalmers Reproservice
Gothenburg, Sweden 2023

Numerical study of nucleate boiling
Diffuse interface simulations of steam bubble departures from superheated wall
ADAM JOHANSSON
Department of Mechanics and Maritime Sciences
Chalmers University of Technology

Abstract

Nucleate boiling is a type of boiling which is characterised by the nucleation, growth and rise of vapour bubbles at the superheated surface. Because latent heat is typically much larger than sensible heat, the heat transfer associated with nucleate boiling is much larger than that of other forms of liquid cooling. Despite its importance, the effect of the wall and fluid properties on heat transfer is not yet fully understood, due to the several mechanisms involved and the many governing parameters. In a field where experiments are cumbersome and hard to realise, numerical simulations are of out most importance to increase our understanding. Here we investigate the effect of contact angle θ_w, wall superheat temperature ΔT and number of nucleation sites N_{bub} on the departure of boiling steam bubbles in quiescent liquid water by means of a novel Diffuse Interface (DI) algorithm for weakly compressible flows. More specifically we estimate the time-averaged Nusselt number, quantifying the non-dimensional wall heat flux. The maximum time averaged Nusselt number was found for $\Delta T = 2.5\,\mathrm{K}$, $\theta_w = 45°$ and $N_{bub} = 1$, which was the lowest superheat temperature, smallest contact angle and lowest number of nucleation sites that were tested. However these results are to be taken with reservations since the simulated bubbles were of several orders of magnitude larger than physical bubble nuclei, probably underestimating the effect of phase change on heat transfer. More work is required to obtain an algorithm that is stable enough to simulate a wider range of parameters.

Keywords: boiling, phase change, diffuse interface, bubble, heat transfer, nucleate boiling, contact angle.

Acknowledgements

I wish to thank my supervisor professor Luca Brandt for all the support and engagement during the work on the thesis. Special thanks to Dr. Armin Shahmardi for all the help, supervision and advice during all stages of the project. Also many thanks to the other colleagues in the KTH mechanics department, especially room mate Dr. Vishal Agrawal for our many fruitful discussions and your guidance.

This thesis also marks the end of a five year long journey through Teknisk Fysik and Applied Mechanics to becoming a Civilingenjör. Therefore I would also want to thank my family who have supported me during all these years. Thanks to my mother Annika for being someone I can always talk to. Thanks to my sister Ellen for being the best possible little sister in the world and thanks to my dad Göran for being an inspiration and showing me the importance of a physical understanding in everything I do. I also want to thanks my friends from Teknisk Fysik for our incredible time together. I would have dropped out a long time ago without you. A special honouring of Sixten Elehed who should have graduated with us. We will never forget you.

Lastly I want to thank my amazing girlfriend Alba for always being there for me and spreading so much joy in my life.

Adam Johansson, Stockholm, May 2023

List of Acronyms

Below is the list of acronyms that have been used throughout this thesis listed in alphabetical order:

CFD	Computational Fluid Dynamics
CHF	Critical Heat Flux
DI	Diffuse Interface
EOS	Equation of State
HTC	Heat transfer coefficient
NASG	Noble-Able stiffened-gas
RK3	Third order Runge-Kutta

Nomenclature

Below is the nomenclature of indices, symbols and non-dimensional numbers that have been used throughout this thesis.

Indices

i	Indices for spatial components of vector quantities
k	Indices for phasic quantities
n	Time step
m	Sub time step
$*$	Index for fractional step prediction
$\dagger$	Index for value after phase transition

Symbols

α_k	Volume fraction
$\tilde{\alpha}_m$	RK3 coefficients
b_k	Phasic parameter of the EOS
$\tilde{\beta}_m$	RK3 coefficients
Γ_r	Regularisation velocity scale parameter
Γ_k	Grüneisen coefficient
γ_k	Phasic parameter of the EOS
$\tilde{\gamma}_m$	RK3 coefficients
C_{pk}	Extensive phasic heat capacity
$C_{\Delta t}$	Courant number
c	Mixture speed of sound
$D_{\mathcal{E}}$	Divergence of viscous dissipation
D_{u_i}	Divergence of viscous stress tensor

d_0	Initial bubble diameter
ϵ	Small tolerance
ε	Interface thickness
$\mathcal{E}$	Mixture internal energy per unit volume
$\mathcal{E}_k$	Internal energy per unit volume
η_k	Phasic heat bond
$\overline{\eta_k}$	Entropy constant
f	Kernel function
G_i	Gravitiational force per unit volume
g_i	Gravitiational acceleration
g_k	Gibbs free energy
h	Heat transfer coefficient
h_k	Specific enthalpy
θ_w	Static contact-angle
κ	Heat conduction coefficient
κ_{pk}	Specific heat capacity at constant pressure
κ_{vk}	Specific heat capacity at constant volume
K	Heat conduction
$\mathcal{L}_{w,k}$	Lagrange multiplier
l_x	Domain size in x-direction
l_y	Domain size in y-direction
μ	Dynamic viscosity
$\mathcal{M}$	Mass transfer term
m_k	Mass per unit volume
ν	Chemical relaxation parameter
N_{bub}	Number of nucleation sites
N_x	Number of grid points in x-direction
N_y	Number of grid points in y-direction
n_i	Interface normal vector
p	Pressure
$p_{\infty k}$	Phasic parameter of the EOS
q	Heat flux
ρ	Mixture density
ρ_k	Phasic density

Σ_i	Surface tension force per unit volume
σ_i	Surface tension coefficient
S_p	Pressure source term
S_T	Temperature source term
s_k	Specific entropy
τ_{ij}	Viscous stress tensor
T	Temperature
ΔT	Superheat temperature
t	Time
u_i	Velocity
x_i	Space coordinates
Ψ	Level-set function

Non-dimensional numbers

Eo	Eötvös number
Fr	Froude number
Ja	Jakob number
λ_κ	Heat conductvity ratio
λ_μ	Viscosity ratio
λ_ρ	Density ratio
Nu	Nusselt number
Re	Reynolds number
We	Weber number

Contents

List of Figures

List of Tables

1

Introduction

The global demand for energy is ever rising and a sustainable solution to meet the demand calls for a multitude technical improvements and innovations. One part in this solution is the increase in efficiency of both generation and consumption of energy [1]. Both energy producing industries such as solar energy and thermal power, and the energy consuming field of electronics require efficient and fast heat transfer [2]. The most efficient way to increase heat transfer is often through phase change since the latent heat involved in the phase transition is generally much larger than the sensible heat. Recent advancements in micro- and nanotechnologies enables high-resolution control of surface properties which influences phase transitions such as boiling and condensation. To utilise this control to manufacture surfaces with optimum characteristics more experimental and theoretical knowledge about the physical phenomena involved is needed [1].

In this thesis the bubbles formed during boiling at a superheated wall will be studied computationally. The heat transfer from wall to fluid together with the dynamical behaviour and phase change of the bubbles will be investigated through numerical simulations. More specifically the effect of wettability, superheat temperature and number of nucleation sites will be probed. In the remainder of this chapter a more extensive background of the project will be presented, followed by the project objective.

1.1 Background

A multiphase flow is a fluid dynamical flow containing two or more thermodynamic phases [3]. Frequently these phases are found to be of separate states of matter, e.g. liquid and gas flow, however generally this is no constraint with oil and water flow being one example of same state of matter multiphase flow. Multiphase flows are present in a multitude of different fields, with examples such as power generation, heat exchangers, sediment transport, food industry, water treatment and the biomedical sector [4]. It is present in virtually all processing technologies, from cavitation in turbines and pumps to the creation of plastics and paper-making. Natural phenomena includes the formation of clouds, avalanches, land slides, fog, snow, to name a few [5]. Moreover, it plays a vital role in biology with the flow of blood

cells (as one of the most important examples) as well as complex dynamics of the membrane of prokaryotic and eukaryotic cells [6].

There are a wide range of complexities connected to multiphase flows, with the broad spectrum of scales and how to handle the interaction between different phases being two major issues. The wide range of scales, where behaviour on the metre or kilometre scale demands capturing and the smallest phenomena occuring on the nano-scale, leads to modelling challenges [5]. It also means that separation of scales can not be guaranteed, which imposes further complications regarding the underlying assumptions in the governing equations. Another challenging aspect of studying multiphase flow systems is the dynamical interactions between phases, with possibility of mass transfer between the phases. A typical example of mass transfer is phase change, which consists of various thermo-physical phenomena mostly governed by variation of state variables of the system such as pressure and temperature.

Phase changes involve the absorption or release of latent heat, which is of interest from a perspective of heat transfer and cooling. In general, phase change phenomena can be categorised into six groups, namely, freezing (transition from liquid to solid phase), deposition (solidification of gaseous phase), melting (solid phase converting to liquid phase), condensation (gaseous phase liquefies), sublimation (solid material changing directly into gaseous phase) and vaporisation (transition from liquid to gaseous phase). There are two types of vaporisation: evaporation and boiling. Evaporation occurs below the boiling point, but only at the surface of a liquid, whereas the bulk phenomenon boiling occurs when a liquid reaches its boiling point.

Heat transfer by the means of boiling is utilised in a wide variety of technological applications such as electronics cooling, heat exchangers and water cooled nuclear reactors to name a few. Despite its widespread use, boiling and how it is effected by the formation of bubbles, is a complex phenomenon that is still not fully understood. The reason for this is the different kinds of mechanisms responsible for heat transfer depending on the flow field and the large numbers of variables affecting the process. Compared to single phase heat transfer we have additional parameters such as latent heat of vaporisation, surface tension, saturation temperature and vapour density [2].

In general, boiling occurs when the liquid temperature reaches the saturation temperature at a given pressure, i.e. the vapour pressure being equal to the surrounding pressure. Vapour can form in the bulk of the liquid, called homogeneous nucleation, for example by microwave heating of an already superheated liquid. The most common way of nucleation is however heterogenous nucleation, meaning that bubbles form either from pre-existing gas nuclei in the bulk of the liquid or at impurities or cavities at the heated surface. These initiation locations are called nucleation sites. As long as the wall temperature is above the saturation temperature boiling can occur, either with the liquid being at the saturation temperature as well (saturated boiling) or with the liquid temperature being below the saturation temperature (subcooled boiling). Boiling can also be divided into two categories depending on the flow field of the fluid above the superheated surface. These are pool boiling, the

case when the fluid above the wall is initialy stagnant, and flow boiling, meaning that the fluid is forced over the surface by e.g. a pump.

Pool boiling is widely used, and espcially a sub-category called nucleate pool boiling, which is known for its high heat transfer coefficients. There are different regimes of pool boiling, depending on i.a. the wall superheat temperature, where nucleate boiling is just one of them. The Figure 1.1, from Faghri and Zhang [7], presents the pool boiling curve which shows the correlation between superheat temperature and wall heat flux for water at atmospheric pressure. For the lowest wall superheat temperatures, natural convection is occuring and no vapour bubbles are formed at the wall. An increase of superheat temperature leads to the nucleation of vapour bubbles at the wall, marking the start of the nucleate boiling regime. For an increased heat flux and wall temperature the frequency, both spatially and temporally, of bubble nucleation increases. Initially the heat transfer is governed by a combination of natural convection and vapour bubbles, where the convection acts in the regions between the bubbles. An increase of wall temperature leads to the bubble nucleation being so profound that it completely dominates the heat transfer, this is the point for maximum heat flux. Additional increase of temperature is followed by reaching the so called critical heat flux (CHF), where the nucleation site density becomes high enough for spots of vapour film to form on the surface, denoting the start of the transition boiling regime. This is followed by a drastic decrease in heat flux due to the insulating gas, if the wall is held at a constant temperature, or an increase in wall temperature if the heat flux is fixed. A point of minimum heat flux is reached called the Leidenfrost point, where the vapour forms a film over the entire surface, and after that the heat flux is once again increased [2]. In this study we will investigate nucleate boiling regime because of the very high heat transfer in relation to superheat temperature.

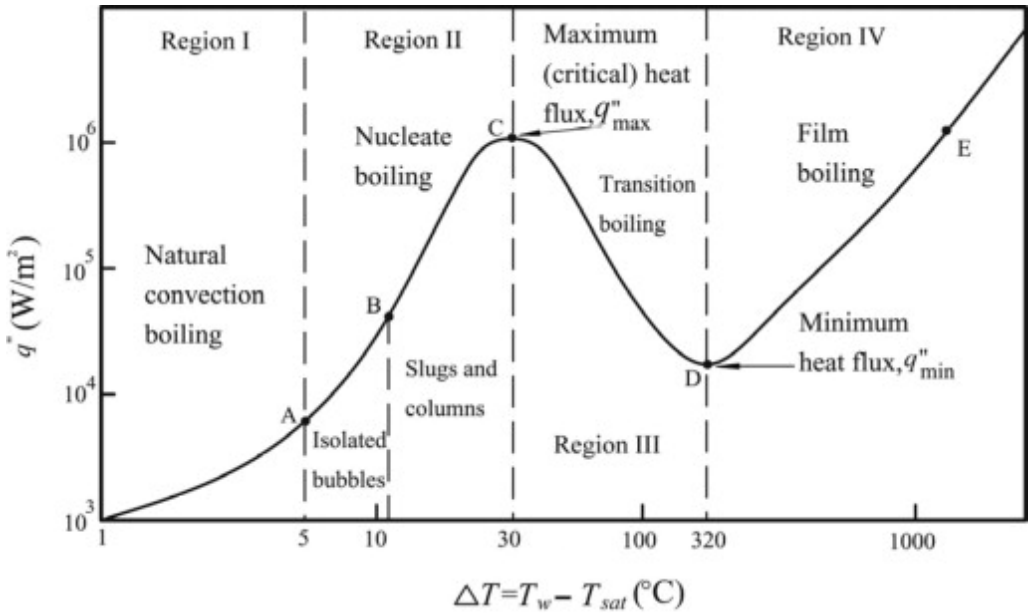

Figure 1.1: Plot of wall heat flux versus wall superheat temperature for pool boiling [7].

To extend our knowledge within this field theory, experiments and numerical simulations have been used by researchers. The underlying theory is crucial for setting up and interpreting the results of both experiments and simulations. Experiments are vital for verifying mathematical models and simulation methods. They have also been fruitful in observing and explaining boiling phenomena. Van Ouwerkerk [8] studied pool boiling and observed dry areas on the heating surface when the critical heat flux was approached. Yu et. al. [9] studied heat transfer from water boiling on horizontal surfaces at sub-atmospheric pressures and reported an increase in heat transfer for increasing pressure. The effect of contact angle on CHF was investigated by Liao et. al. [10] and their results suggest an increase in CHF for increasingly hydrophilic surfaces. A very fascinating phenomenon was observed by Rahman, Pollack and McCarthy when they organised bubble nucleation sites in rows by spatially varying the wall temperature. A 5x increase of heat transfer due to resonance effects was observed at a given superheat temperature for wall temperature variations with spatial wavelength approximately equal to the capillary length [11].

Experiments are however cumbersome and there are limitations on the level of detail of the results obtained, with surface tension being a hard measured quantity. Theory also has restrictions, with many assumptions being made. Therefore high-fidelity numerical simulations are important tools to contribute to the deep understanding of the underlying mechanisms [12]. During the last decades, a variety of numerical frameworks have been introduced by different researchers aiming at understanding more details of multiphase systems and in particular boiling heat transfer. On the smallest scales molecular dynamics simulations are utilised to understand the behaviour of multiphase phenomena such as the interface between water and vapour, where the length and time scales are much smaller then those of the flow field [13]. Then there are are methods based on microscopic models and mesoscopic kinetic equations, with the main example being the Lattice Boltzmann method [14]. In this method the underlying theory is based on the kinetic theory of gases instead of the continuum description. Finally we have the family of methods whose frameworks are building on the continuum description of the fluid and solving the Navier-Stokes equations. These methods can be divided into one fluid- and two fluid-methods. In the two fluid-method, termed Eulerian-Eulerian, both phases are modelled as continua and are fully interpenetrating, making the detailed information about the interface lost [15]. Single fluid-methods apply a single set of governing equations in the entire domain, representing the different phases with different phasic properties, e.g. density, viscosity and heat conduction. This set of equations is also valid at the interface between phases, but this comes with a new set of challenges [16]. In this project a method belonging to the latter group will be used for our simulations.

One of the most challenging tasks in numerical simulations of multiphase flows is that of simulating the interface between two or more phases. The challenges arises from the fact that the width of the interface is of the molecular length scale, much smaller than the length scale of interest in the fluid. Even if we would try to perform simulations on that length scale the continuum description would be violated, rendering the chosen simulation framework not valid. Five main challenges are identified connected to the interface: ensuring conservation of mass, momentum

and kinetic energy, modelling large discontinuities of properties such as density over the interface, guarantee separation of scales and handling complex topologies, correct implementation of surface tension forces and finally achieving robust simulations of realistic flows [17]. To deal with these issues, one first has to keep track of the interface. How this is done is mainly divided into two categories: interface-tracking and interface-capturing. The former approach is implemented by marking the interface with a set of Lagrangian points and tracking the movement of said points, hence the name. Examples of methods taking this approach are the Immersed Boundary Method [18] and Front Tracking [19]. In the latter approach the interface is instead captured by the use of an indicator function, defined on the same Eulerian mesh as the governing equations. This indicator function varies between different values in different phases and the interface is captured by monitoring where the indicator function yields intermediate values. Both approaches have advantages and disadvantages, and the suitable method has to be chosen depending on the studied problem. For this study an interface-capturing approach is utilised, with one on the main advantages being the absence of Lagrangian points needed to be tracked.

Interface-capturing techniques can be divided into two main categories depending on how the interface is represented: sharp interface methods and diffuse interface (DI) methods. In sharp interface methods the fluid properties jump sharply across the interface, whereas in DI methods the physical properties are functions of the phase indicator function and varies smoothly [17]. Examples of two prominent sharp interface methods are volume-of-fluid methods [20] and level-set methods [21]. In this project however we will resolve to using a DI method, which present some advantages in compressible mulitphase flows despite the drawbacks connected to the interface being significantly larger than the physical interface. One of the advantages is that the thermodynamic consistency is kept everywhere, even at the interface. The overall stability and accuracy is also benefited from that the increased resolution in the numerical calculations of the property gradients due to the diffused interface. Lastly, the merging and detaching of interfaces occurs naturally, which is a great advantage in boiling simulations [22].

The Baer-Nunziato model [23] is the most general form of two-phase DI model. It consists of seven equations: two mass conservation equations (one for each phase), two momentum conservation equations, two total energy conservation equations and one volume fraction evolution equation. This model is what is called a non-equilibrium model since there is no requirement for kinetic, mechanical, thermal or chemical equilibrium where the two phases coexist. With other words, the two phases do not need to have same velocity, pressure, temperature or Gibbs free energy in those regions. By the relaxation of said quantities different models can be derived, depending on the problem at hand. For problems governed by conductive heat transfer, a four equation model introduced by Abgrall [24] is well suited. This model imposed kinetic, mechanical and thermal equilibrium. Phase change is modelled by a procedure of relaxing Gibbs free energy. To solve this model an algorithm developed by Demou *et al.* [22] will be used. The idea behind this numerical methodology is combining the pressure-based approach from incompressible flow and applying this to flows with phase change, which are compressible altough at low

Mach numbers. This algorithm was further improved by Shahmardi [4] by adding interface regularistation and contact angle functionality.

Using this novel algorithm the behaviour of boiling bubbles will be investigated. The effect of contact angle, density of nucleation sites and superheat temperature is to be analysed, both on the growth and detachment of the bubbles and the heat flux from the wall to the fluid. The existence of an optimum configuration of parameters that allows for maximum heat flux coefficient, i.e. ratio of wall heat flux to superheat temperature, will be probed. For measure the dimensionless Nusselt number Nu will be used, normalising the heat flux coefficient with a characteristic length scale and heat conduction coefficient.

The hypothesis is that there will be an optimum amount of bubble contact with the wall for maximum amount of heat transfer due to phase change. On one hand we have hydrophilic contact angles, which allow for quick bubble detachments and large contact of the liquid water with the wall, leading to high amount of conductive heat transfer due to the high heat conductivity of the liquid phase. On the other hand we have hydrophobic contact angles which allows for slow bubble departures with potentially large amounts of heat transfer due to absorption of latent heat. The arguments for nucleation site densities are similar, with the trade-off between conductive and phase change heat transfer to be considered. Here the possibly of observing resonance between bubbles also exists. Regarding the superheat temperature, an increase of it will increase the heat flux until the critical heat flux and initiation of film boiling.

1.2 Project objective

The aim of this project is two-folded. The first goal is to further continue development of an in-house numerical code for studying phase change and learn more about the complications of applying Computational Fluid Dynamics (CFD) skills in modelling complex multiphase flow systems. Next, we aim at analysing the behaviour of water vapour bubbles in quiescent liquid water at saturation temperature, departing from a superheated wall. The analysis will be done by performing numerical simulations using a four equation diffuse interface model with phase change. In particular the heat flux will be studied and a maximum is tried to be found.

2

Mathematical model

This thesis project, as mentioned in the introduction, investigates nucleate boiling by numerical simulations using a four equation DI model with phase change. Firstly in this chapter, in Section 2.1 the governing equations of the model will be introduced without phase change. In Section 2.2 the equation of state will be introduced and in Section 2.3 the details about the phase change are to be unveiled. Thereafter in 2.4 the method for interface regularisation is discussed and finally the method for handling the contact line is disclosed in 2.5.

2.1 Governing equations

As introduced in the previous chapter, the description of the two phase flow used in this thesis project is a diffuse interface model based on the original seven equation Baer-Nunziato model [23], but with relaxation of velocity, pressure and temperature. This four-equation model where the flow is in thermal, mechanical and kinetic equilibrium, was originally introduced by Abgrall [24]. For solving this system of equations, a pressure-based algorithm presented by Demou *et al.* [22] and improved by Shahmardi [4] is used. This model is an augmented four-equation model solving for five variables, i.e. the masses of both phases are explicitly solved for. Since kinetic, mechanical and thermodynamic equilibrium are imposed, the velocity u_i, the temperature T, and the pressure p are the same for the two phases where they coexist. In this chapter the governing equations are presented in their original form without phase change. For details about the phase change see section 2.3. The governing equations reads as follows [12]:

$$\frac{\partial m_1}{\partial t} + \frac{\partial}{\partial x_i}(m_1 u_i) = 0, \tag{2.1a}$$

$$\frac{\partial m_2}{\partial t} + \frac{\partial}{\partial x_i}(m_2 u_i) = 0, \tag{2.1b}$$

$$\frac{\partial T}{\partial t} + \frac{\partial}{\partial x_i}(T u_i) + \left(S_T^{(1)} - T\right)\frac{\partial u_j}{\partial x_j} = S_T^{(2)}(D_{\mathcal{E}} + K), \tag{2.1c}$$

$$\frac{\partial u_i}{\partial t} + \frac{\partial}{\partial x_j}(u_i u_j) - u_i\frac{\partial u_j}{\partial x_j} = \frac{1}{\rho}(D_{u_i} + \Sigma_i + G_i), \tag{2.1d}$$

$$\frac{\partial p}{\partial t} + u_i\frac{\partial p}{\partial x_i} + \rho c^2\frac{\partial u_i}{\partial x_i} = S_p^{(1)}(D_{\mathcal{E}} + K), \tag{2.1e}$$

here $m_k = \alpha_k \rho_k$ is the mass per unit volume of phase k, where $k = 1, 2$, α_k the volume fraction, ρ_k the phase density, t is time and x_i are space coordinates.

The temperature and pressure source terms S_T and S_p are:

$$\begin{aligned} S_T^{(1)} &= \frac{\rho c^2 T}{C_{p1} + C_{p2}} \left(\frac{C_{p1}\Gamma_1}{\rho_1 c_1^2} + \frac{C_{p2}\Gamma_2}{\rho_2 c_2^2} \right), \\ S_T^{(2)} &= -\frac{1}{\overline{D}} (\zeta \rho)^T, \\ S_p^{(1)} &= \frac{1}{\overline{D}} (\phi \rho)^T, \end{aligned} \tag{2.2}$$

where we have the mixture density $\rho = \alpha_1 \rho_1 + \alpha_2 \rho_2$, speed of sound of the mixture c, extensive heat capacity at constant pressure for phase k, C_{pk}, and the Grüneisen coefficient $\Gamma_k = \left(\frac{\partial p_k}{\partial \mathcal{E}_k} \right)_{\rho_k}$. Here $\mathcal{E}_k$ is the internal energy per unit volume for each phase. The mixture speed of sound is defined as:

$$\frac{1}{c^2} = \rho \left(\frac{\alpha_1}{\rho_1 c_1^2} + \frac{\alpha_2}{\rho_2 c_2^2} \right) + \frac{\rho T C_{p1} C_{p2}}{C_{p1} + C_{p2}} \left(\frac{\Gamma_2}{\rho_2 c_2^2} - \frac{\Gamma_1}{\rho_1 c_1^2} \right)^2. \tag{2.3}$$

Further we have:

$$\begin{aligned} \overline{D} &= \left(\frac{\rho_1 c_1^2}{\Gamma_1} - \frac{\rho_2 c_2^2}{\Gamma_2} \right) (\phi \zeta)^T + \left(\frac{\alpha_1}{\Gamma_1} + \frac{\alpha_2}{\Gamma_2} \right) (\phi \rho)^T, \\ (\zeta \rho)^T &= \alpha_1 \zeta_1 \rho_2 + \alpha_2 \zeta_2 \rho_1, \\ (\phi \rho)^T &= \alpha_1 \phi_1 \rho_2 + \alpha_2 \phi_2 \rho_1, \\ (\phi \zeta)^T &= \alpha_1 \alpha_2 (\phi_1 \zeta_2 - \phi_2 \zeta_1), \end{aligned} \tag{2.4}$$

where

$$\phi_k = \left(\frac{\partial \rho_k}{\partial T_k} \right)_{p_k} = -\rho_k \frac{\Gamma_k C_{pk}}{c_k^2 \alpha_k \rho_k} \tag{2.5}$$

and

$$\zeta_k = \left(\frac{\partial \rho_k}{\partial p_k} \right)_{T_k} = \frac{1}{c_k^2} + \frac{\Gamma_k^2 C_{pk} T}{c_k^4 \alpha_k \rho_k}. \tag{2.6}$$

We furthermore have the divergence of the viscous stress tensor D_{u_i} and viscous dissipation $D_{\mathcal{E}}$:

$$\begin{aligned} D_{u_i} &= \frac{\partial}{\partial x_j} \tau_{ij}, \\ D_{\mathcal{E}} &= \frac{\partial}{\partial x_i} u_j \tau_{ij}, \\ \tau_{ij} &= \mu \left(\frac{\partial u_i}{\partial x_j} + \frac{\partial u_j}{\partial x_i} - \frac{2}{3} \frac{\partial}{\partial x_k} u_k \delta_{ij} \right), \end{aligned} \tag{2.7}$$

where τ_{ij} is the viscous stress tensor, μ is the dynamic viscosity and σ_{ij} is the Kronecker delta. Note that we have assumed a Newtonian constitutive relation for the viscous stress tensor.

$K = \frac{\partial}{\partial x_i}(\kappa)\frac{\partial T}{\partial x_i}$ is the heat conduction given by Fourier's law, where κ is the coefficient of heat conduction, and $G_i = \rho g_i$ is the gravitational force per unit volume where g_i is the gravitational acceleration.

Finally we have the surface tension force per unit volume [25]:

$$\Sigma_i = \sigma \frac{\partial}{\partial x_j}\left(\frac{\frac{\partial \alpha_1}{\partial x_j}}{\sqrt{(\frac{\partial \alpha_1}{\partial x_k}\frac{\partial \alpha_1}{\partial x_k})}}\right)\frac{\partial \alpha_1}{\partial x_i}, \tag{2.8}$$

where σ is the coefficient of surface tension.

2.2 Equation of state

For closure of the system of equations presented in the previous chapter an equation of state (EOS) for each phase is needed. The EOS for the mixture is determined from the individual equation of states by the mixture density relation $\rho = \alpha_1\rho_1 + \alpha_2\rho_2$, mixture internal energy relation per unit volume $\mathcal{E} = \alpha_1\mathcal{E}_1 + \alpha_2\mathcal{E}_2$, temperature equilibrium condition $T_1 = T_2 = T$ and pressure equilibrium condition $p_1 = p_2 = p$. In this project the Noble-Able stiffened-gas (NASG) EOS has been used [26]. The temperature and pressure are in this model expressed as [22]:

$$T_k(p_k, \rho_k) = \frac{(1-\rho_k b_k)(p_k + p_{\infty k})}{\kappa_{vk}\rho_k(\gamma_k - 1)}, \tag{2.9a}$$

$$p_k(\mathcal{E}_k, \rho_k) = \frac{\gamma_k - 1}{1-\rho_k b_k}(\mathcal{E}_k - \eta_k\rho_k) - \gamma_k p_{\infty k}, \tag{2.9b}$$

where b_k, $p_{\infty k}$, γ_k, η_k, are phasic parameters of the EOS and κ_{vk} is the phasic specific heat capacity at constant volume. Note that the extensive heat capacity is $C_{pk} = \alpha_k\rho_k\kappa_{pk}$ where $\kappa_{pk} = \kappa_{vk}\gamma_k$. Equation 2.9a is used to obtain the phasic densities ρ_k by first using 2.1c and 2.1e to solve for p and T and then relaxing the pressure, $p_k = p$, and temperature $T_k = T$. With the above expressions, the phasic Grüneisen coefficient Γ_k, speed of sound c_k, Gibbs energy g_k, specific enthalpy h_k and specific entropy s_k become:

$$\Gamma_k(\rho_k) = \frac{\gamma_k - 1}{1-\rho_k b_k}, \tag{2.10a}$$

$$c_k(p, \rho_k) = \sqrt{\gamma_k \frac{p + p_{\infty k}}{\rho_k(1-\rho_k b_k)}}, \tag{2.10b}$$

$$g_k(p, \rho_k) = (\gamma_k\kappa_{vk} - \tilde{\eta}_k)T - \kappa_{vk}T\log\left(\frac{T^{\gamma_k}}{(p+p_{\infty k})^{\gamma_k - 1}}\right) + \eta_k + b_k p, \tag{2.10c}$$

$$h_k(p, T) = \kappa_{pk}T + b_k p + \eta_k, \tag{2.10d}$$

$$s_k(p, T) = \kappa_{vk}\log\left(\frac{T^{\gamma_k}}{(p+p_{\infty k})^{\gamma_k - 1}}\right) + \tilde{\eta}_k, \tag{2.10e}$$

where $\tilde{\eta}_k$ is an entropy constant.

The equation of state for each phase is used to obtain the pressure-temperature saturation curve for the fluid by using that Gibbs free energy is in equilibrium along the curve, setting $g_1 = g_2$. After inserting the expressions above and rewriting, the final expression for the curve is given by:

$$A_s = \frac{B_s}{T} + C_s \log T + D_s \log(p + p_{\infty 1}) - \log(p + p_{\infty 2}) + \frac{pE_s}{T} = 0, \tag{2.11}$$

where,

$$\begin{aligned} A_s &= \frac{\kappa_{p1} - \kappa_{p2} - \tilde{\eta}_1 + \tilde{\eta}_2}{\kappa_{p2} - \kappa_v 2}, B_s = \frac{\eta_1 - \eta_2}{\kappa_{p2} - \kappa_{v2}}, C_s = \frac{\kappa_{p1} - \kappa_{v1}}{\kappa_{p2} - \kappa_{v2}}, \\ D_s &= \frac{\kappa_{p1} - \kappa_{v1}}{\kappa_{p2} - \kappa_{v2}} \text{ and } E_s = \frac{b_1 - b_2}{\kappa_{p2} - \kappa_v 2}. \end{aligned} \tag{2.12}$$

This curve is used for determining the saturation temperature and pressure for all positions in the domain, controlling the phase change that will be discussed in detail in the next chapter.

2.3 Phase change

In the previous section, it was discussed how equation 2.1 was closed using the NASG equation of state. From it the pressure-temperature saturation curve was obtained to calculate the saturation temperature for the given pressure. Using this saturation temperature, the phase change can be modelled. This is done through modifying equation 2.1, by adding mass transfer terms to the right hand side of the mass, temperature and pressure transportation equations [12]:

$$\mathcal{M} = \nu(g_2 - g_1) \tag{2.13}$$

where ν represents the chemical relaxation parameter and g is the Gibbs free energy [22]. With the mass transfer, the full system of equations solved reads as follows:

$$\begin{aligned} \frac{\partial m_1}{\partial t} + \frac{\partial}{\partial x_i}(m_1 u_i) &= \mathcal{M}, \\ \frac{\partial m_2}{\partial t} + \frac{\partial}{\partial x_i}(m_2 u_i) &= -\mathcal{M}, \\ \frac{\partial T}{\partial t} + \frac{\partial}{\partial x_i}(T u_i) + \left(S_T^{(1)} - T\right)\frac{\partial u_j}{\partial x_j} &= S_T^{(2)}(D_{\mathcal{E}} + K) + S_T^{(3)}\mathcal{M}, \\ \frac{\partial u_i}{\partial t} + \frac{\partial}{\partial x_j}(u_i u_j) - u_i\frac{\partial u_j}{\partial x_j} &= \frac{1}{\rho}(D_{u_i} + \Sigma_i + G_i), \\ \frac{\partial p}{\partial t} + u_i\frac{\partial p}{\partial x_i} + \rho c^2\frac{\partial u_i}{\partial x_i} &= S_p^{(1)}(D_{\mathcal{E}} + K) + S_p^{(2)}\mathcal{M}, \end{aligned} \tag{2.14}$$

where the new quantities $S_T^{(3)}$ and $S_p^{(2)}$ are defined as:

$$\begin{aligned} S_T^{(3)} &= \frac{1}{\overline{\overline{D}}}\left[\left(\frac{\chi_2}{\Gamma_2}-\frac{\chi_1}{\Gamma_1}\right)(\zeta\rho)^T+\left(\frac{\rho_1 c_1^2}{\Gamma_1}-\frac{\rho_2 c_2^2}{\Gamma_2}\right)\zeta_v+\left(\frac{\alpha_1}{\Gamma_1}+\frac{\alpha_2}{\Gamma_2}\right)\Delta\rho\right], \\ S_p^{(2)} &= \frac{1}{\overline{\overline{D}}}\left[\left(\frac{\chi_1}{\Gamma_1}-\frac{\chi_2}{\Gamma_2}\right)(\phi\rho)^T+\left(\frac{\rho_2 c_2^2}{\Gamma_2}-\frac{\rho_1 c_1^2}{\Gamma_1}\right)\phi_v\right], \end{aligned} \tag{2.15}$$

where

$$\begin{aligned} \Delta\rho &= \rho_2-\rho_1, \\ \phi_v &= \alpha_1\phi_1+\alpha_2\phi_2, \\ \zeta_v &= \alpha_1\zeta_1+\alpha_2\zeta_2, \\ \chi_k &= c_k^2-\Gamma_k h_k. \end{aligned} \tag{2.16}$$

2.4 Interface regularisation

Diffuse interface methods suffers under a well known drawback: the interface spreads over many computational cells. A remedy to this is the usage of anti-diffusion techniques. The model used in this projects follows the approach of Jain [27] and introduces interface regularisation in the mass transport equations. With the regularisation included, these equations are written as:

$$\frac{\partial m_1}{\partial t}+\frac{\partial}{\partial x_i}(m_1 u_i)=\mathcal{M}+\frac{\partial}{\partial x_i}R_i(\alpha_1,\rho_1), \tag{2.17a}$$

$$\frac{\partial m_2}{\partial t}+\frac{\partial}{\partial x_i}(m_2 u_i)=-\mathcal{M}+\frac{\partial}{\partial x_i}R_i(\alpha_2,\rho_2), \tag{2.17b}$$

where $R_i(\alpha_1,\rho_1)$ is an *Accurate Conservative Diffuse Interface* (ACDI) regularisation term and is expressed as:

$$R_i(\alpha_1,\rho_1)=\Gamma_r\varepsilon\rho_1\frac{\partial\alpha_1}{\partial x_i}-\frac{\Gamma_r\rho_1}{4}\left(1-\tanh^2\left(\frac{\psi}{2\varepsilon}\right)\right)n_i, \tag{2.18}$$

where ε is the interface thickness, Γ_r is the regularisation velocity scale parameter and

$$\psi=\varepsilon\ln\left(\frac{\alpha_1+\epsilon}{1-\alpha_1+\epsilon}\right) \tag{2.19}$$

is a level-set function where $\epsilon=2\cdot10^{-16}$ is a small tolerance and

$$n_i=\frac{\frac{\partial\psi}{\partial x_i}}{\sqrt{\frac{\partial\psi}{\partial x_j}\frac{\partial\psi}{\partial x_j}}} \tag{2.20}$$

is the interface normal vector. Boundedness of the indicator function, $0 < \alpha_1 < 1$ is ensured with proper values of ε and Γ_r, and are chosen accordingly to Jain [27]:

$$\begin{aligned} \Gamma_r &> |u_i|_{max} \\ \varepsilon &> 0.5\Delta x, \end{aligned} \tag{2.21}$$

where $|u_i|_{max}$ is the maximum magnitude of the velocity field and Δx is the size of the grid.

2.5 Contact line treatment

Another important physical phenomenon to model is the contact line where the interface between the two phases meets the wall. This is in this project done by enforcing a static contact-angle θ_w boundary condition on the wall normal gradient of the phasic masses m_k. This boundary condition is derived by Shahmardi [4] from the Cahn-Hilliard framework's conventional static contact angle boundary conditions [28]:

$$\frac{\partial \alpha_1}{\partial x_i} n_i = \frac{f^{'}}{\varepsilon}(\alpha_1)\cos(\theta_w), \tag{2.22}$$

where $f(\alpha_1) = 3\alpha_1^2 - 2\alpha_1^3$ is a kernel function that varies smoothly between 0 and 1 within the interface. Using $\alpha_1 = m_1/\rho_1$ we write the left hand side of 2.22 as:

$$\frac{\partial \alpha_1}{\partial x_1} n_i = \frac{1}{\rho_1}\frac{\partial m_1}{\partial x_i} n_i - \frac{m_1}{\rho_1^2}\frac{\partial \rho_1}{\partial x_i} n_i. \tag{2.23}$$

Inserting this left hand side and rearranging the terms yields the final boundary condition that is used in the model:

$$\frac{\partial m_1}{\partial x_i} n_i = \rho_1 \frac{f^{'}}{\varepsilon}(\alpha_1)\cos(\theta_w) + \frac{m_1}{\rho_1}\frac{\partial \rho_1}{\partial x_i} n_i. \tag{2.24}$$

Since the original Cahn-Hilliard formulation is a fourth order equation an additional boundary condition is imposed at the wall to ensure mass conservation. The model used in this project is a second order equation and therefore another constraint is needed to ensure that the total mass of the system is conserved. This is done by employing Lagrange multipliers $\mathcal{L}_{w,k}$ to the right-hand-side of the mass transport equations [29]. E.g. the transport equation for m_1 becomes:

$$\frac{\partial m_1}{\partial t} + \frac{\partial}{\partial x_i}(m_1 u_i) = M + \frac{\partial}{\partial x_i} R_i(\alpha_1, \rho_1) + \mathcal{L}_{w,1}. \tag{2.25}$$

We assume $\mathcal{L}_{w,k} = q_k(t)\mathcal{W}(\alpha_k, \rho_k)$ where q_k is a function constant in space and $\mathcal{W} = \rho_k f^{'}(\alpha_1)$ is a kernel function. To calculate $q(t)$ we integrate the mass transport equations over the domain and enforce the total mass of the two phases to be conserved, yielding the following expression:

$$q_k(t) = -\frac{1}{\int_\Omega 6\rho_k\alpha_k(1-\alpha_k)d\Omega}\int_\Omega \frac{\partial}{\partial x_i}R_i(\alpha_1,\rho_1)d\Omega. \tag{2.26}$$

Combining the four-equation model, mass transfer, contact line and regularisation gives the final set of governing equations solved in the project:

$$\frac{\partial m_1}{\partial t} + \frac{\partial}{\partial x_i}(m_1 u_i) = \mathcal{M} + \frac{\partial}{\partial x_i}R_i(\alpha_1,\rho_1) + \mathcal{L}_{w,1}, \tag{2.27a}$$

$$\frac{\partial m_2}{\partial t} + \frac{\partial}{\partial x_i}(m_2 u_i) = -\mathcal{M} + \frac{\partial}{\partial x_i}R_i(\alpha_2,\rho_2) + \mathcal{L}_{w,2}, \tag{2.27b}$$

$$\frac{\partial T}{\partial t} + \frac{\partial}{\partial x_i}(T u_i) + \left(S_T^{(1)} - T\right)\frac{\partial u_j}{\partial x_j} = S_T^{(2)}(D_\mathcal{E} + K) + S_T^{(3)}\mathcal{M}, \tag{2.27c}$$

$$\frac{\partial u_i}{\partial t} + \frac{\partial}{\partial x_j}(u_i u_j) - u_i\frac{\partial u_j}{\partial x_j} = \frac{1}{\rho}\left(D_{u_i} + \Sigma_i + G_i\right), \tag{2.27d}$$

$$\frac{\partial p}{\partial t} + u_i\frac{\partial p}{\partial x_i} + \rho c^2\frac{\partial u_i}{\partial x_i} = S_p^{(1)}(D_\mathcal{E} + K) + S_p^{(2)}\mathcal{M}. \tag{2.27e}$$

3

Numerical methods

In this section the details about the numerical solution of the governing equations 2.27 will be presented. The algorithm operates in the following way, and the chapter will be organised in similar fashion. First the system of equations in 2.27 consisting of the mass transport, momentum , energy and pressure is solved, but without the terms containing $\mathcal{M}$. Next, to include the role of phase change, the source term $\mathcal{M}$ in equations 2.27a, 2.27b, 2.27c and 2.27e is integrated in time. Therefore first the spatial discretisation and time integration without mass transfer will discussed in Section 3.1. Thereafter the numerics of the phase transition will be explained in Section 3.2 and lastly in Section 3.3 the conditions for the variable time step will be stated.

3.1 Solution method without mass transfer

In the present study, we borrow the idea of Demou *et al.* [22] and employ a pressure based algorithm to solve the governing equations presented in the previous chapter. In this section the numerical steps will be shown that are done without incorporating the phase change. In each time step this algorithm is run before being corrected by the mass transfer term presented in the next chapter.

3.1.1 Spatial and temporal discretisation

The governing equations 2.27 are spatially discretised on a uniform Cartesian grid with the cell lengths being $\Delta x = l_x/N_x$, $\Delta y = l_y/N_y$ and $\Delta z = l_z/N_z$, where the domain lengths are l_x, l_y, and l_z and the number of cells are N_x, N_y and N_z. To avoid pressure-velocity oscillations a staggered grid is used where the velocity vectors are defined on the cell faces and all scalar fields defined at the cell centres. For the spatial discretisation a second-order finite difference scheme is used.

Time integration is performed using the explicit third order Runga-Kutta (RK3) method. The RK3 method works by splitting each time step n into three sub-steps $m = 1, 2, 3$ and any quantity a at the beginning and end of each time-step is represented using the following the notation [22]:

$$a^{n,m=1} = a^n \quad \text{and} \quad a^{n,m=4} = a^{n+1}. \tag{3.1}$$

3.1.2 Partial densities

Firstly partial densities of the new sub-step $m_k^{n,m+1}$ are solved for by using the mass transport equations 2.27a and 2.27b, without the mass transfer terms $\mathcal{M}$. Accordingly to the RK3 method the updated $m_k^{n,m+1}$ is given by:

$$\begin{aligned} m_k^{n,m+1} = m_k^{n,m} + \Delta t \Bigg[& \tilde{\alpha}^m \left(-\frac{\partial}{\partial x_i}(m_k u_i) \right)^{n,m} + \\ & \tilde{\beta}^m \left(-\frac{\partial}{\partial x_i}(m_k u_i) \right)^{n,m-1} + \\ & \tilde{\gamma}^m \left(\frac{\partial}{\partial x_i} R_i(\alpha_k, \rho_k) + \mathcal{L}_{w,k} \right) \Bigg], \end{aligned} \tag{3.2}$$

where Δt is the time step, $\tilde{\alpha}^m = \{8/15, 5/12, 3/4\}$, $\tilde{\beta}^m = \{0, -17/60, -5/12\}$ and $\tilde{\gamma}^m = \tilde{\alpha}^m + \tilde{\beta}^m$ are RK3 coefficients. The advection terms, regularisation and Lagrange multiplier are discretised with central differences.

3.1.3 Temperature, physical properties and curvature

Secondly the temperature field is advanced in time similar to the partial densities. The temperature equation 2.27c, without $\mathcal{M}$, is solved to obtain the next sub-step of $T^{n,m+1}$ [22]:

$$\begin{aligned} T^{n,m+1} = T^{n,m} + \Delta t \Bigg[& \tilde{\alpha}^m \left(-\frac{\partial}{\partial x_i}(T u_i) - \left(S_T^{(1} - T \right) \frac{\partial u_i}{\partial x_i} \right)^{n,m} + \\ & \tilde{\beta}^m \left(-\frac{\partial}{\partial x_i}(T u_i) - \left(S_T^{(1} - T \right) \frac{\partial u_i}{\partial x_i} \right)^{n,m-1} + \\ & \tilde{\gamma}^m \left(S_T^{(2} (D_{\mathcal{E}} + K) \right)^{n,m} \Bigg]. \end{aligned} \tag{3.3}$$

A van Leer flux limiter is used to discretise the advection terms while the viscous dissipation and heat conduction terms are discretised with central differences.

Thereafter the fields of of viscosity and thermal conductivity are updated as:

$$\mu^{n,m+1} = \alpha_1^{n,m+1}\mu_1 + \alpha_2^{n,m+1}\mu_2 \quad \text{and} \quad \lambda^{n,m+1} = \alpha_1^{n,m+1}\lambda_1 + \alpha_2^{n,m+1}\lambda_2 \tag{3.4}$$

where $\alpha_2 = 1 - \alpha_1$ and $\mu_1, \mu_2, \lambda_1, \lambda_2$ are constant [22].

3.1.4 Fractional Step

In addition to the staggered grid a fractional-step approach is adopted to decouple pressure and velocity [30] [22]. That means that we firstly calculate a predicted velocity field $u_i^{n,m*}$ by solving the momentum equation Eq. (2.27d), omitting the pressure gradient term.

3.1.4.1 Predicted velocity

The predicted velocity $u_i^{n,m*}$ is expressed as:

$$u_i^{n,m*} = u_i^{n,m} + \Delta t \Bigg[\tilde{\alpha}^m \left(-\frac{\partial}{\partial x_j}(u_i u_j) + u_i \frac{\partial u_j}{\partial x_j} + \frac{D_{u_i}}{\rho} \right)^{n,m} + \tilde{\beta}^m \left(-\frac{\partial}{\partial x_j}(u_i u_j) + u_i \frac{\partial u_j}{\partial x_j} + \frac{D_{u_i}}{\rho} \right)^{n,m-1} + \tilde{\gamma}^m \left(\frac{\Sigma_i + G_i}{\rho} \right)^{n,m} \Bigg]. \tag{3.5}$$

All terms are discretised in the same manners as before.

3.1.4.2 Correction

The corrected updated velocity field $u_i^{n,m+1}$ can be calculated once the updated pressure field $p^{n,m+1}$ is obtained and is given by the following expression:

$$u_i^{n,m+1} = u_i^{n,m*} - \tilde{\gamma}^m \Delta t \frac{\partial p^{n,m+1}}{\partial x_i} / \rho^{n,m} \tag{3.6}$$

.

3.1.4.3 Pressure solution

Thereafter the time discretisation of the pressure equation Eq. (2.27e), without $\mathcal{M}$, is written as:

$$p^{n,m+1} = p^{n,m} + \Delta t \Bigg[\tilde{\alpha}^m \left(-\frac{\partial}{\partial x_i}(p u_i) + p \frac{\partial u_i}{\partial x_i} \right)^{n,m} + \tilde{\beta}^m \left(-\frac{\partial}{\partial x_i}(p u_i) + p \frac{\partial u_i}{\partial x_i} \right)^{n,m-1} + \tilde{\gamma}^m \left\{ \left(S_p^{(1}(D_{\mathcal{E}} + K) \right)^{n,m} - (\rho c^2)^{n,m} \left(\frac{\partial u_i}{\partial x_i} \right)^{n,m+1} \right\} \Bigg], \tag{3.7}$$

with the discretisation performed as above. Now the last velocity divergence term is replaced by the divergence of Eq. (3.6):

$$\left(\frac{\partial u_i}{\partial x_i} \right)^{n,m+1} = \left(\frac{\partial u_i}{\partial x_i} \right)^{n,m*} - \tilde{\gamma}^m \Delta t \frac{\partial}{\partial x_i} \left(\frac{\partial p^{n,m+1}}{\partial x_i} / \rho^{n,m} \right). \tag{3.8}$$

Inserting Eq. (3.8) in Eq. (3.7) gives:

$$\begin{aligned} p^{n,m+1} - ((\tilde{\gamma}^m)^2 \Delta t^2 \rho c^2)^{n,m} \left(\frac{\partial u_i}{\partial x_i}\right)^{n,m+1} = \\ p^{n,m} + \Delta t \Bigg[\tilde{\alpha}^m \left(-\frac{\partial}{\partial x_i}(p u_i) + p \frac{\partial u_i}{\partial x_i} \right)^{n,m} + \\ \tilde{\beta}^m \left(-\frac{\partial}{\partial x_i}(p u_i) + p \frac{\partial u_i}{\partial x_i} \right)^{n,m-1} + \\ \tilde{\gamma}^m \left\{ \left(S_p^{(1}(D_{\mathcal{E}} + K) \right)^{n,m} - (\rho c^2)^{n,m} \left(\frac{\partial u_i}{\partial x_i} \right)^{n,m*} \right\} \Bigg], \end{aligned} \tag{3.9}$$

which is a Helmholtz equation. This Helmholtz equation is solved using the HYPRE library [31].

3.2 Phase transition

An operator splitting technique is used to implement the phase change term $\mathcal{M}$. As explained in the previous chapter the governing equations are first solved without $\mathcal{M}$ to get $m_k^{n,m+1}$, $T^{n,m+1}$ and $p^{n,m+1}$ which actually are intermediate values. We here denote $m_k^{n,m+1+\dagger}$, $T^{n,m+1+\dagger}$ and $p^{n,m+1+\dagger}$ as the actual value at the next time step. At the end of each stage the independent variables are updated using the strategy proposed by Pelanti [32]:

$$m_1^{n,m+1+\dagger} = m_1^{n,m+1} + \frac{g_2^{n,m+1} - g_1^{n,m+1}}{K_g}(1 - \exp(-\nu K_g \Delta t)), \tag{3.10a}$$

$$p^{n,m+1+\dagger} = p^{n,m+1} + S_p^{(2)} \frac{g_2^{n,m+1} - g_1^{n,m+1}}{K_g}(1 - \exp(-\nu K_g \Delta t)), \tag{3.10b}$$

$$T^{n,m+1+\dagger} = T^{n,m+1} + S_T^{(3)} \frac{g_2^{n,m+1} - g_1^{n,m+1}}{K_g}(1 - \exp(-\nu K_g \Delta t)), \tag{3.10c}$$

where $K_g = 1/\xi_1^{n,m+1} + 1/\xi_2^{n,m+1}$ and $1/\xi_k^{n,m+1} = (-1)^{k-1} S_p^{(2)}/\rho_k - s_k S_T^{(3)}$ for $k = 1, 2$. To enforce exact global mass conservation we update $m_2^{n,m+1+\dagger} = \rho^{n,m+1+\dagger} - m_1^{n,m+1+\dagger}$ which works since ρ is invariant during each mass transfer time step. In this project we set the chemical relaxation parameter $\nu = \infty$, i.e. we have instaneous mass transfer.

3.3 Time step

Compared to implicit time integration schemes, explicit schemes demand smaller time steps to stay stable. To only use as small time step as necessary a variable time step restriction is implemented. This is done accordingly to [22] and [33]:

$$\Delta t = C_{\Delta t} \min(\Delta t_c, \Delta t_\sigma, \Delta t_\mu, \Delta t_\lambda), \tag{3.11}$$

where $C_{\Delta t}$ is the Courant number and $\Delta t_c, \Delta t_\sigma, \Delta t_\mu, \Delta t_\lambda$ are the upper limits of the time step with regards to convection, surface tension, momentum and thermal energy diffusion. These maximum time steps are given by the following expressions:

$$\begin{aligned}
\Delta t_c &= \left(\frac{|u_{x,max}|}{\Delta x} + \frac{|u_{y,max}|}{\Delta y} + \frac{|u_{z,max}|}{\Delta z} \right)^{-1}, \\
\Delta t_\sigma &= \sqrt{\frac{(\rho_{1,min} + \rho_{2,min}) \min(\Delta x^3, \Delta y^3, \Delta z^3)}{4\pi\sigma}}, \\
\Delta t_\mu &= \left[\max\left(\frac{\mu_1}{\rho_{1,min}}, \frac{\mu_2}{\rho_{2,min}} \right) \left(\frac{2}{\Delta x^2} + \frac{2}{\Delta y^2} + \frac{2}{\Delta z^2} \right) \right]^{-1} \\
\Delta t_\lambda &= \left[\max\left(\frac{\lambda_1}{\rho_{1,min} C_{p,1}}, \frac{\lambda_2}{\rho_{2,min} C_{p,2}} \right) \left(\frac{2}{\Delta x^2} + \frac{2}{\Delta y^2} + \frac{2}{\Delta z^2} \right) \right]^{-1},
\end{aligned} \tag{3.12}$$

where we have the estimation of the velocity component with the largest absolute value $|u_{i,max}|$ and the minimum value of the density of phase k in the domain ρ_k.

4

Results and discussion

In the previous chapters a mathematical model for describing two-phase flows was presented. This model combined mass transfer due to phase change with wettability effects on the contact angle. Then the numerical methods for discretising and solving the equations in time and space was presented. This section will present the results of solving this model for a range of different cases. We consider the boiling of a rising bubble as a benchmark. In Section 4.1 the simulation setup of the benchmark case will be presented. In the present study, we focus on the role of different superheat temperature, different surface chemistry (wettability), and different number of nucleation sites on the dynamics of a boiling rising bubble. To better understand the effects of the above mentioned properties, we keep all the setup parameters as the ones of the benchmark case and change only one at the time. In particular, in Section 4.2, we scrutinise the role of wall superheat temperatures, in Section 4.3 we investigate the effect of the wettability and finally Section 4.4 addresses the effects of the number of nucleation sites per unit length. The results of each section are compared both qualitatively (by reporting the system visualisations) and qualitatively (via comparing the non-dimensional heat flux) . The chapter is summarised by a heat map of the average Nusselt number for all the setups in Section 4.5 and finished by a discussion about the results and method in Section 4.6.

4.1 Setup

As presented in Section 2.2, the NASG equations of state are used in this project. The corresponding thermodynamic properties of a liquid water and steam system is presented in the following table:

Coefficients	Liquid Phase	Vapour Phase
$\kappa_p(J/kg/K)$	4285	1401
$\kappa_v(J/kg/K)$	3610	955
γ	1.19	1.47
$p_\infty(Pa)$	7028×10^5	0
$b(m^3/kg)$	6.61×10^-4	0
η	-1177788	2077616
$\tilde{\eta}$	0	14317

Table 4.1: Thermo-physical properties of the system.

These values are valid for water vapour and liquid water in the temperature range of $[300 - 500\,\mathrm{K}]$ and all the simulations in this project are within this temperature range. The initial setup is shown in the following Figure 4.1, where the dark area shows the initial steam bubble and the remainder of the domain is liquid water.

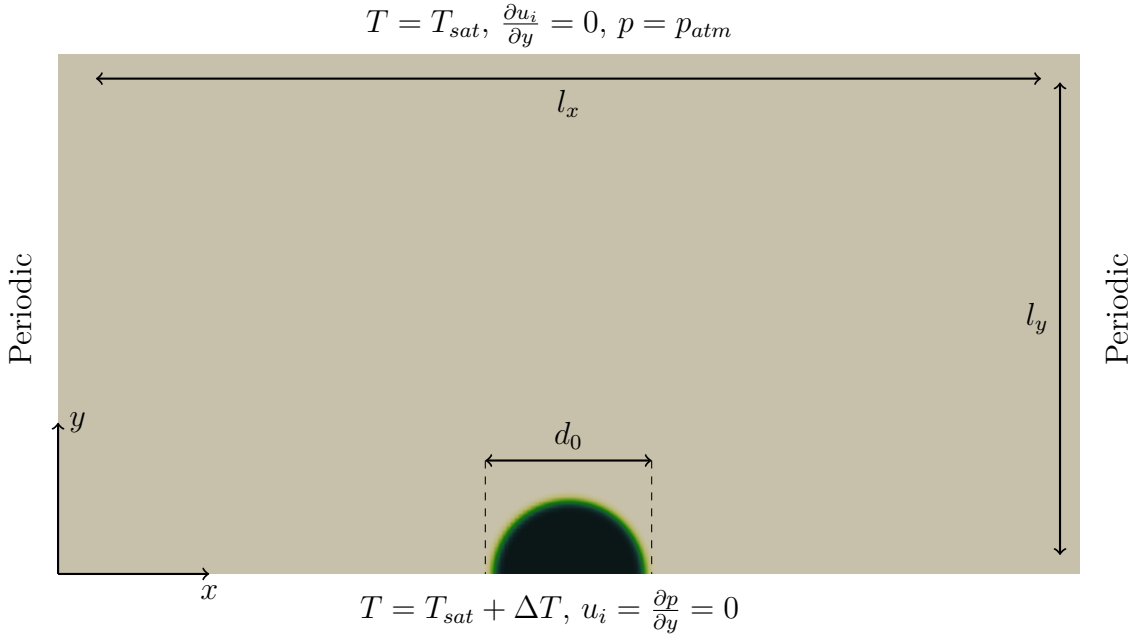

Figure 4.1: Initial state of the benchmark case. Volume fraction of steam is visualised with dark area indicating vapour and bright area liquid water. Initial diameter d_0 is shown as well as the coordinate axes x and y. The arrows l_x and l_y indicate the domain lengths. Boundary conditions for temperature T, velocity components u_i and pressure p are specified at respective boundary.

The two dimensional domain size is set to $l_x \times l_y = 7d_0 \times 3.5d_0 = 0.07\,\mathrm{m} \times 0.035\,\mathrm{m}$, where $d_0 = 0.01\,\mathrm{m}$ is the initial bubble diameter. Further the domain is discretised with $N_x \times N_y = 128 \times 64$ grid points. Initial pressure in the entire domain is set uniformly to atmospheric pressure, $p_0 = p_{atm} = 101325\,\mathrm{Pa}$. Both phases are

initialised at saturation temperature, determined from the equation of state, i.e, $T_0 = 372.585\,\mathrm{K}$. The fluid is initialised at rest and gravitational acceleration is set to $g = -9.81\,\mathrm{m/s^2}$ in y-direction. In this chapter we denote the vapour phase as $k = 1$ and the liquid phase as $k = 2$. Viscosities are set to the following: $\mu_1 = 0.001\,\mathrm{Pa \cdot s}$, $\mu_2 = 0.01\,\mathrm{Pa \cdot s}$ and thermal conductivity coefficients to $\kappa_1 = 0.0249\,\mathrm{W/(m \cdot K)}$, $\kappa_2 = 0.60\,\mathrm{W/(m \cdot K)}$. At any state of the system (given the pressure and temperature) the value of the density of each phase is obtained via the EOS, where the initial values being $\rho_{1,0} = 0.7574\,\mathrm{kg/m^3}$ and $\rho_{2,0} = 1054\,\mathrm{kg/m^3}$. Surface tension is set to $\sigma = 0.07\,\mathrm{N/m}$. The regularisation velocity scale is set to $\Gamma_r = 5|u_i|_{max}$ and interface thickness $\varepsilon = 0.51\Delta x$.

All simulations are performed in a two dimensional setup and periodic boundary conditions are enforced in the x-direction. The lower boundary is set to represent a wall with homogeneous Dirichlet conditions for all the velocity components u_i. Dirichlet boundary conditions also apply for the temperature $T_{y=0} = T_0 + \Delta T$, with ΔT being the superheat temperature. To enforce the contact angle the boundary condition from Eq. 2.24 is enforced for the phasic masses. For pressure p, level-set function Ψ, interface normal vector n_i and density ρ, homogeneous Neumann boundary conditions apply. An outflow boundary condition is imposed on the upper boundary of the simulation domain by imposing Neuman boundary condition for velocity components together with Dirichlet boundary condition for the pressure and the temperature; i.e. $p_{y=ly} = p_{atm}$ and $T_{y=ly} = 372.585\,\mathrm{K}$. We further impose Neumann boundary conditions for the level-set function and interface normal vector.

We introduce the reference length $l_r = d_0$ and the reference velocity to be $u_r = \sqrt{|g|l_r}$. The physical dimensionless parameters that governs the overall dynamics of the system can now be defined as:

$$Re = \frac{\rho_1 u_r d_0}{\mu_1} = 330, \tag{4.1a}$$

$$We = \frac{\rho_1 u_r^2 d_0}{\sigma} = 14.8, \tag{4.1b}$$

$$Fr = \frac{u_r^2}{|g| d_0} = 1, \tag{4.1c}$$

$$Eo = \frac{(\rho_2 - \rho_1) g d_0^2}{\sigma} = 14.8, \tag{4.1d}$$

$$\lambda_\rho = \frac{\rho_2}{\rho_1} = 1391, \tag{4.1e}$$

$$\lambda_\mu = \frac{\mu_2}{\mu_1} = 10, \tag{4.1f}$$

$$\lambda_\kappa = \frac{\kappa_2}{\kappa_1} = 24, \tag{4.1g}$$

$$Ja = \frac{\rho_2}{\rho_1} \frac{\kappa_{p,2} \Delta T}{\Delta h_{lv}}. \tag{4.1h}$$

Here Re is the Reynolds number which is a measure of the ratio between inertial and viscous forces, We the Weber number, measure of inertial to surface tension forces, Fr the Froude number, representing the relative importance of inertial to gravity effects and Eo the Eötvös number stating the balance between gravitational and surface tension forces. Moreover, λ_ρ, λ_μ and λ_κ represent the density, viscosity and heat conductivity ratios, respectively. Finally Ja is the Jakob number and defined as the ration between sensible heat and absorbed latent heat during the phase change. The heat flux q at the lower wall is calculated as:

$$q = -\kappa \frac{\partial T}{\partial y} \tag{4.2}$$

where κ is the mixture heat conductivity. A quantitative measure of the effectiveness of boiling is the heat transfer coefficient (HTC) h, defined as the ratio of heat flux of the surface to the superheat temperature:

$$h = \frac{q}{\Delta T}. \tag{4.3}$$

In our analyses, we report the value of the non dimensional Nusselt number, which is defined as:

$$Nu = \frac{h l_y}{\kappa_2} \tag{4.4}$$

and represents the ratio of convective to conductive heat transfer at the boundary. Finally for presenting the results we utilise the dimensionless time $t^* = t/t_{ff}$, where t is the physical time and $t_{ff} = \sqrt{l_y/|g|}$ is the free-fall time.

4.2 Effect of superheat temperature

To probe the influence of wall superheat temperature on the rise and formation of bubbles six simulations were performed with with superheat temperatures $\Delta T = [2.5\,\mathrm{K}, 5\,\mathrm{K}, 7.5\,\mathrm{K}, 10\,\mathrm{K}, 12.5\,\mathrm{K}, 15\,\mathrm{K}]$. This corresponds to Jakob numbers $Ja = [6.8, 13.7, 20.5, 27.3, 34.2, 41.0]$. The equilibrium contact angle was set to $\theta_w = 120°$ and the bubble was initialised at $(x_{c0}, y_{c0}) = (3.5d_0, 0)$ where x_{c0}, y_{c0} are the centre coordinates of the circular bubble, meaning that our bubble is semi circular due to it being initialised at the bottom wall. In Figure 4.2 the vapour volume fraction can be seen for three different times, $t^* = [0.67, 1.34, 2.0]$, where the results are only shown for superheat temperatures $\Delta T = [5\,\mathrm{K}, 10\,\mathrm{K}, 15\,\mathrm{K}]$ for clarity.

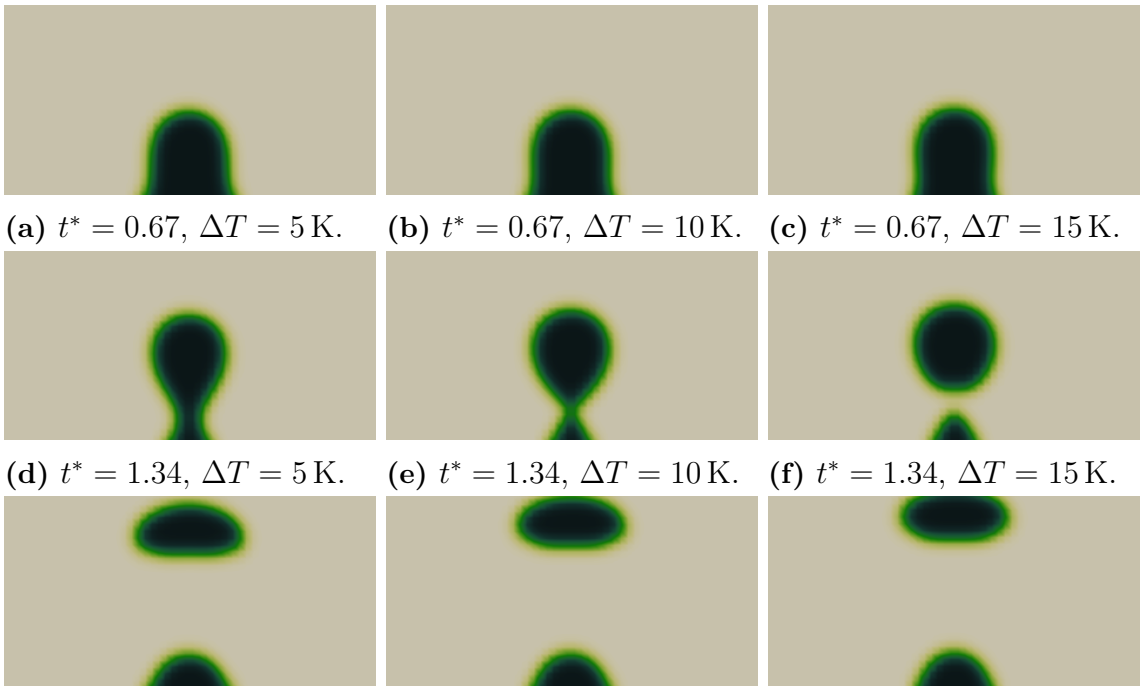

(a) $t^* = 0.67$, $\Delta T = 5\,\mathrm{K}$. **(b)** $t^* = 0.67$, $\Delta T = 10\,\mathrm{K}$. **(c)** $t^* = 0.67$, $\Delta T = 15\,\mathrm{K}$.

(d) $t^* = 1.34$, $\Delta T = 5\,\mathrm{K}$. **(e)** $t^* = 1.34$, $\Delta T = 10\,\mathrm{K}$. **(f)** $t^* = 1.34$, $\Delta T = 15\,\mathrm{K}$.

(g) $t^* = 2.0$, $\Delta T = 5\,\mathrm{K}$. **(h)** $t^* = 2.0$, $\Delta T = 10\,\mathrm{K}$. **(i)** $t^* = 2.0$, $\Delta T = 15\,\mathrm{K}$.

Figure 4.2: Volume fraction of the rising boiling bubble for $\theta_w = 120°$ at times $t^* = 0.67 - 1.34 - 2.0$. Subfigures $(a) - (d) - (g)$ report the results for $\Delta T = 5\,\mathrm{K}$, $(b) - (e) - (h)$ the results for $\Delta T = 10\,\mathrm{K}$ and $(c) - (f) - (i)$ for $\Delta = 15\,\mathrm{K}$.

Figure 4.2 reports the visualisation of the system at three different time instances for each contact angle. Comparing the left, middle, and right panel of Figure 4.2 we observe that as the superheat temperature increases the bubble departs faster. We associate this with buoyancy effects: the larger the super heat, the larger the heat transfer, thus the higher the temperature close to the wall. Thus, as the temperature increases, the gas density decreases further and consequently the rising velocity increases. Moreover, irrespective of the imposed wall superheat temperature, due to hydrophobic property of the wall, the bubble grows on the wall by forming a obtuse contact angle ($\theta_w > 90°$). Finally, there is always some amount of gas left on the solid wall which acts as a potential nucleus for formation and growth of the next bubble.

The heat flux at the wall as a function of time for the different superheat temperatures can be seen in Figure 4.3. Nusselt number Nu and dimensionless time t^* are calculated as explained in Section 4.1. Black dashed line represents $\Delta T = 15\,\mathrm{K}$, green solid line $\Delta T = 10\,\mathrm{K}$ and dash-dotted blue line $\Delta T = 5\,\mathrm{K}$.

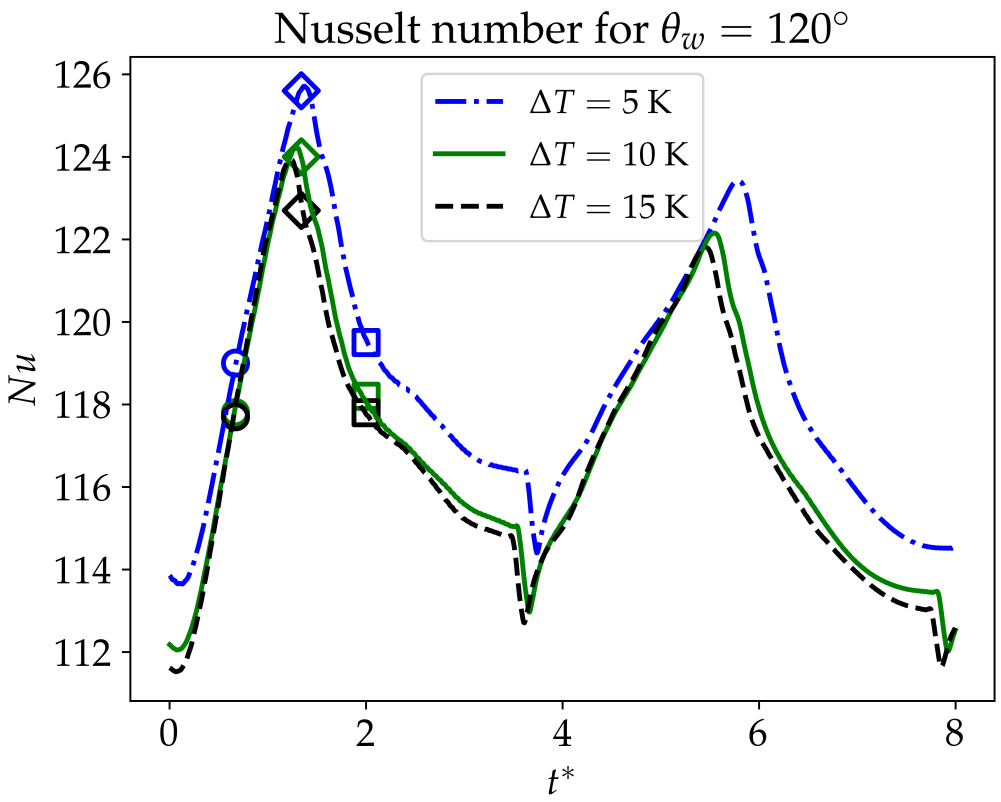

Figure 4.3: Nusselt number $Nu = ql_y/(\kappa_2 \Delta T)$ as function of dimensionless time $t^* = t/\sqrt{l_y/|g|}$ with superheat temperature ΔT as variable parameter. The symbols mark the time steps for the visualisations in 4.2.

Figure 4.3 illustrates the evolution of Nu for the three selected superheat temperature. For each superheat, the time instances corresponding the visualisations in Figure 4.2 are marked with symbols. As the first observation, regardless to the imposed superheat temperature, the heatflux first increases and then decreases. This observation is understood considering the contraction of the bubble as it detaches, thus increasing the liquid-wall contact until a maximum is reached at the departure. Therefore the remaining gas spreads on the surface, having an insulating effect, where the heat transfer decreases dramatically.

In addition, Figure 4.3 suggests that the Nusselt number decreases as the superheat temperature increases. Since the difference in Nusselt number is seen already at initiation and remains approximately constant, this could indicate that the heat transfer due to phase change is constant. That would explain the decrease in Nusselt number since the heat conduction fraction of total heat transfer increases as wall temperature increases. Secondly, we can clearly observe the cyclic behaviour of bubble formation. As it was shown in figure 4.2, due to hydrophobic characteristic of the surface, the bubble departs the surface leaving some residual behind which act as the nucleus of the next bubble which grows again and the cycle continues.

Finally, comparing the distance between the two consecutive peaks in each plot (corresponding to a required time for the bubble to complete each cycle) we observe that as the superheat temperature increases, the cycle becomes shorter. This confirms our previous discussion on figure 4.2: the larger the superheat, the faster the bubble departs. To further investigate the role of superheat on the departure time, we report the variation of the cycle period with superheat in Figure 4.4.

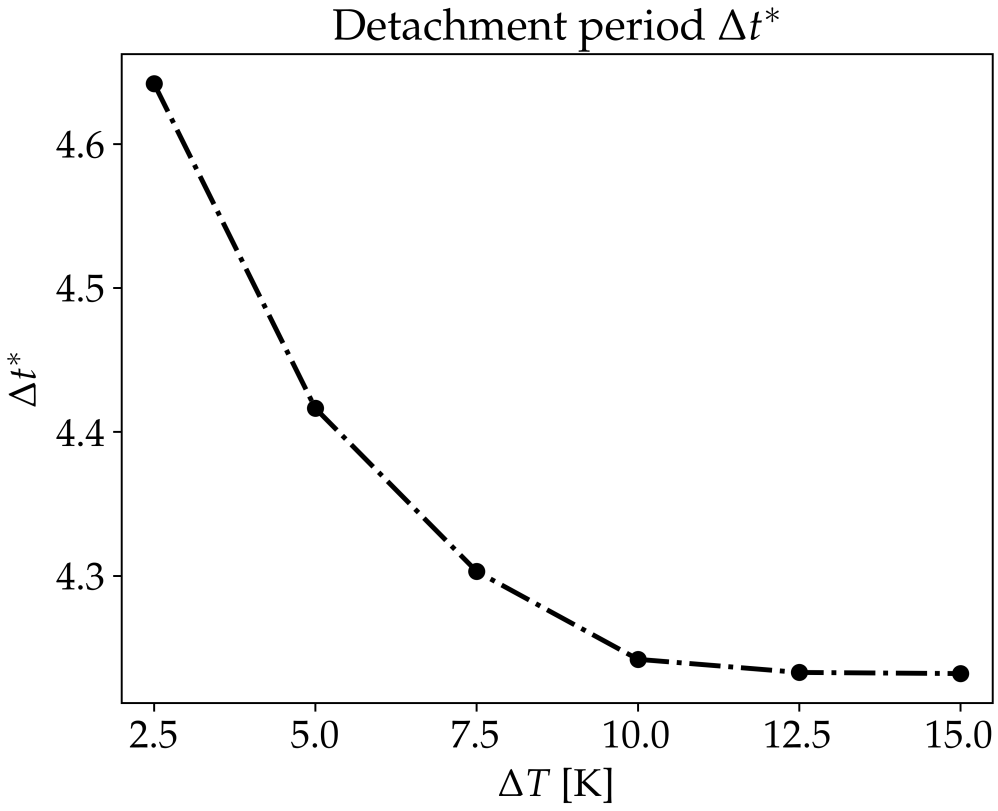

Figure 4.4: Departure cycle period time Δt^* as function of wall superheat temperature for θ.

4.3 Effect of wettability

Another set of simulations were performed with a constant superheat temperature $\Delta T = 15\,\mathrm{K}$ and with varying static contact angle $\theta_w = [45°, 60°, 90°, 120°, 135°]$. This corresponds to Jakob number $Ja = 41$ and the bubble was again initialised at $(x_{c0}, y_{c0}) = (3.5d_0, 0)$. In Figure 4.5 the vapour volume fraction can be seen for four different times, $t^* = [0.39, 0.74, 0.92, 1.34]$, for the respective contact angle.

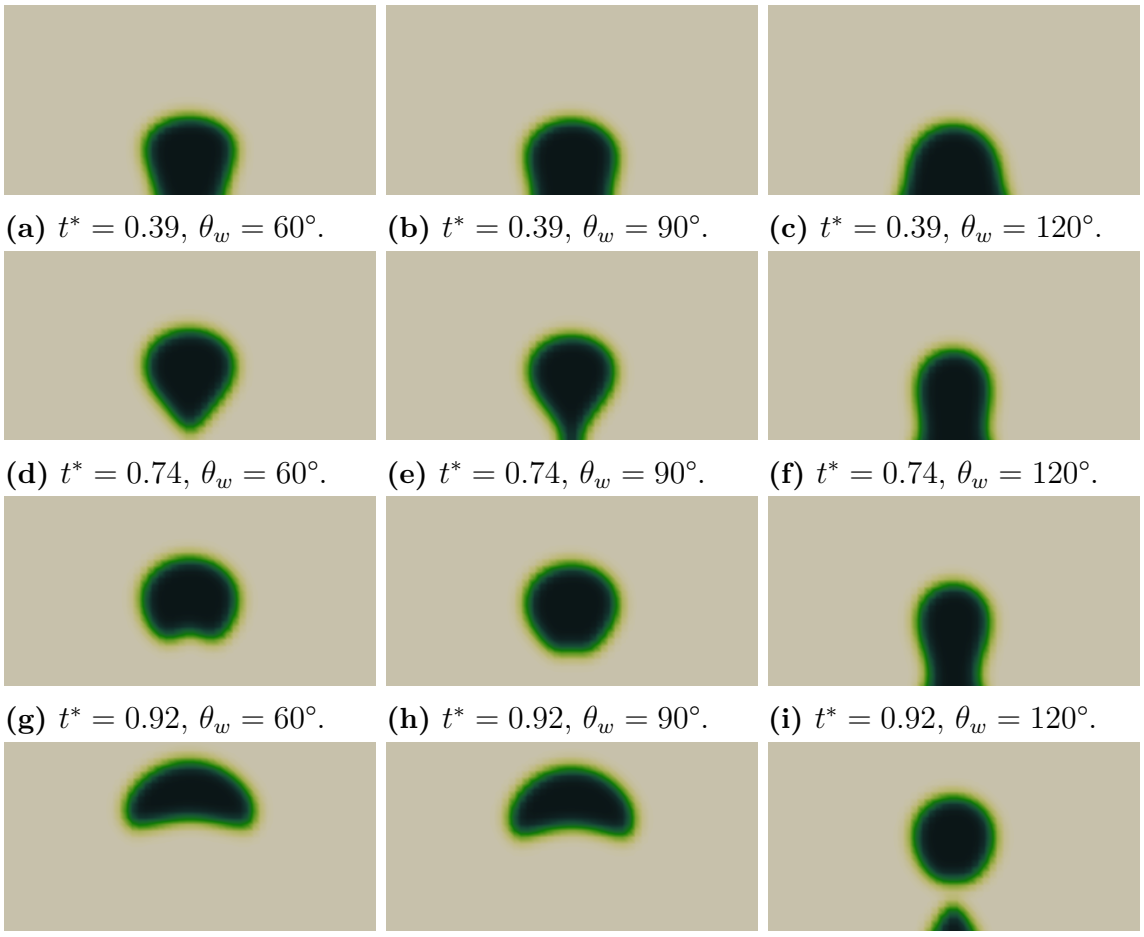

(a) $t^* = 0.39$, $\theta_w = 60°$. **(b)** $t^* = 0.39$, $\theta_w = 90°$. **(c)** $t^* = 0.39$, $\theta_w = 120°$.

(d) $t^* = 0.74$, $\theta_w = 60°$. **(e)** $t^* = 0.74$, $\theta_w = 90°$. **(f)** $t^* = 0.74$, $\theta_w = 120°$.

(g) $t^* = 0.92$, $\theta_w = 60°$. **(h)** $t^* = 0.92$, $\theta_w = 90°$. **(i)** $t^* = 0.92$, $\theta_w = 120°$.

(j) $t^* = 1.34$, $\theta_w = 60°$. **(k)** $t^* = 1.34$, $\theta_w = 90°$. **(l)** $t^* = 1.34$, $\theta_w = 120°$.

Figure 4.5: Volume fraction of the rising boiling bubble for $\Delta T = 15\,\mathrm{K}$ at times $t^* = 0.39 - 0.74 - 0.92 - 1.34$. Subfigures $(a) - (d) - (g) - (j)$ report the results for $\theta_w = 60°$, $(b) - (e) - (h) - (k)$ the results for $\theta_w = 90°$ and $(c) - (f) - (i) - (l)$ for $\theta_w = 120°$.

According to Figure 4.5, the wall chemistry has a dominant role on the overall dynamic of the system. In particular, comparing different columns of Figure 4.5, we conclude that for a hydrophilic wall the bubble departs relatively fast without leaving any residual behind, whereas the bubble departs the hydrophobic wall later, leaving some residual gas phase on the wall. This can be understood by considering the interfacial forces at the wall. A neutral wall shows a similar behaviour as the hydrophilic wall, albeit at a slower rate.

In Figure 4.6 the time evolution of the Nusselt number can be seen for the different values of contact angle. Black dashed line represents $\theta_w = 120°$, green solid line $\theta_w = 90°$ and dash-dotted blue line $\theta_w = 60°$.

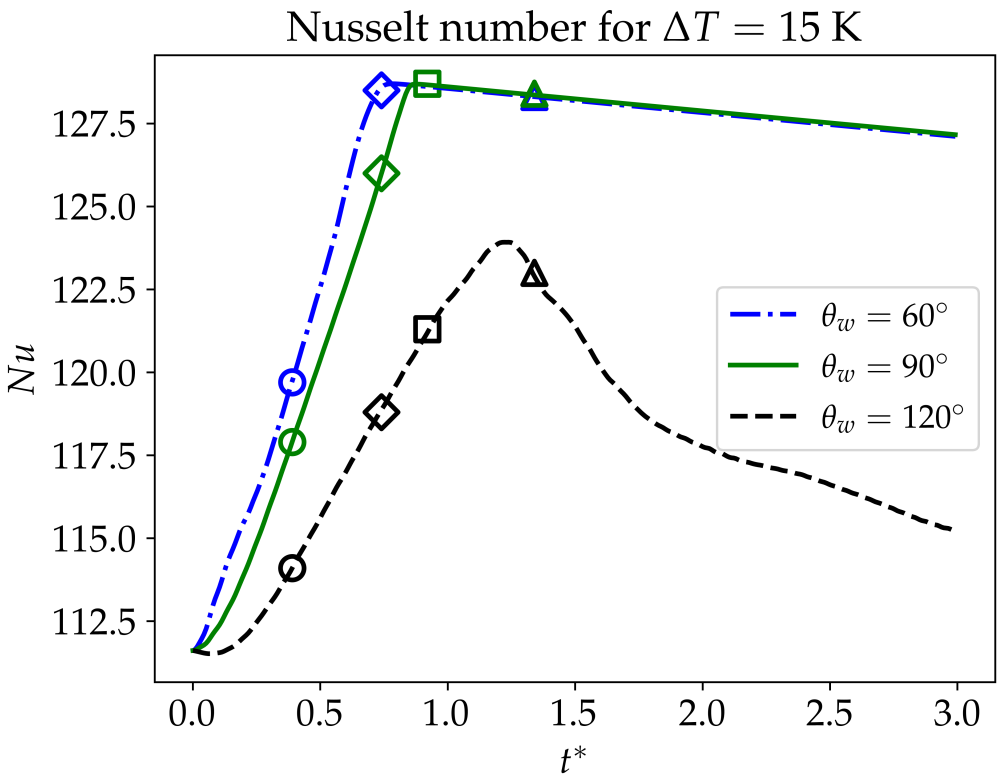

Figure 4.6: Nusselt number $Nu = ql_y/(\kappa_2 \Delta T)$ as function of dimensionless time $t^* = t/\sqrt{l_y/|g|}$ with static contact angle θ_w as variable parameter.

It can be noticed that due to the same initial conditions, the Nusselt number is the same for all angels at $t = 0$. Remember that the bubble was initialised as a perfect semicircle, with an initial contact angle between bubble and wall being 90°, the imposed contact angle taking some time to actually being enforced due to inertia. After the initiation the effect of the contact angle and the subsequent spreading is seen with the heat flux being the lowest for hydrophobic angle $\theta_w = 120°$ (black line) and highest for hydrophilic $\theta_w = 60°$ (blue line), due to the wall having a larger contact area with the highly conducting liquid water for the hydrophilic case leading to higher heat flux. For both $\theta_w = 60°$ and $\theta_w = 90°$ (green line) the heat flux is seen to rapidly increase up to a maximum, for thereafter decreasing linearly. This can be explained by the total detachment of the bubble, with the fluid next to the wall thereafter slowly heating up leading to lower heat flux. The general trend is similar for $\theta_w = 120°$ but the maximum heat flux is lower and reached later due to the slower detachment and the vapour left on the wall. Interesting to note is that the Nusselt number is higher for $\theta_w = 60°$ and $\theta_w = 90°$ compared to $\theta_w = 120°$ even after the complete detachment of the bubbles. This shows that the heat flux for the wall only in contact with liquid water, without phase change, is higher than the combination of phase change with gas-wall contact.

4.4 Effect of number of nucleation sites

Simulation series number three was performed to see the effect of nucleation site density, by varying the number of initial bubbles at the lower boundary. This was done with fixed superheat temperature $\Delta T = 5\,\mathrm{K}$ and static contact angle $\theta_w = 120°$. Since the domain length in x direction was seven times the initial bubble diameter, $l_x = 7d_0$, the number of initial bubbles, N_{bub} were varied between 1 and 7. The resulting steam volume fraction is to be seen in Figure 4.7, for $N_{bub} = [5, 7]$ at times $t^* = [0.52, 2.59, 5.04, 5.86]$.

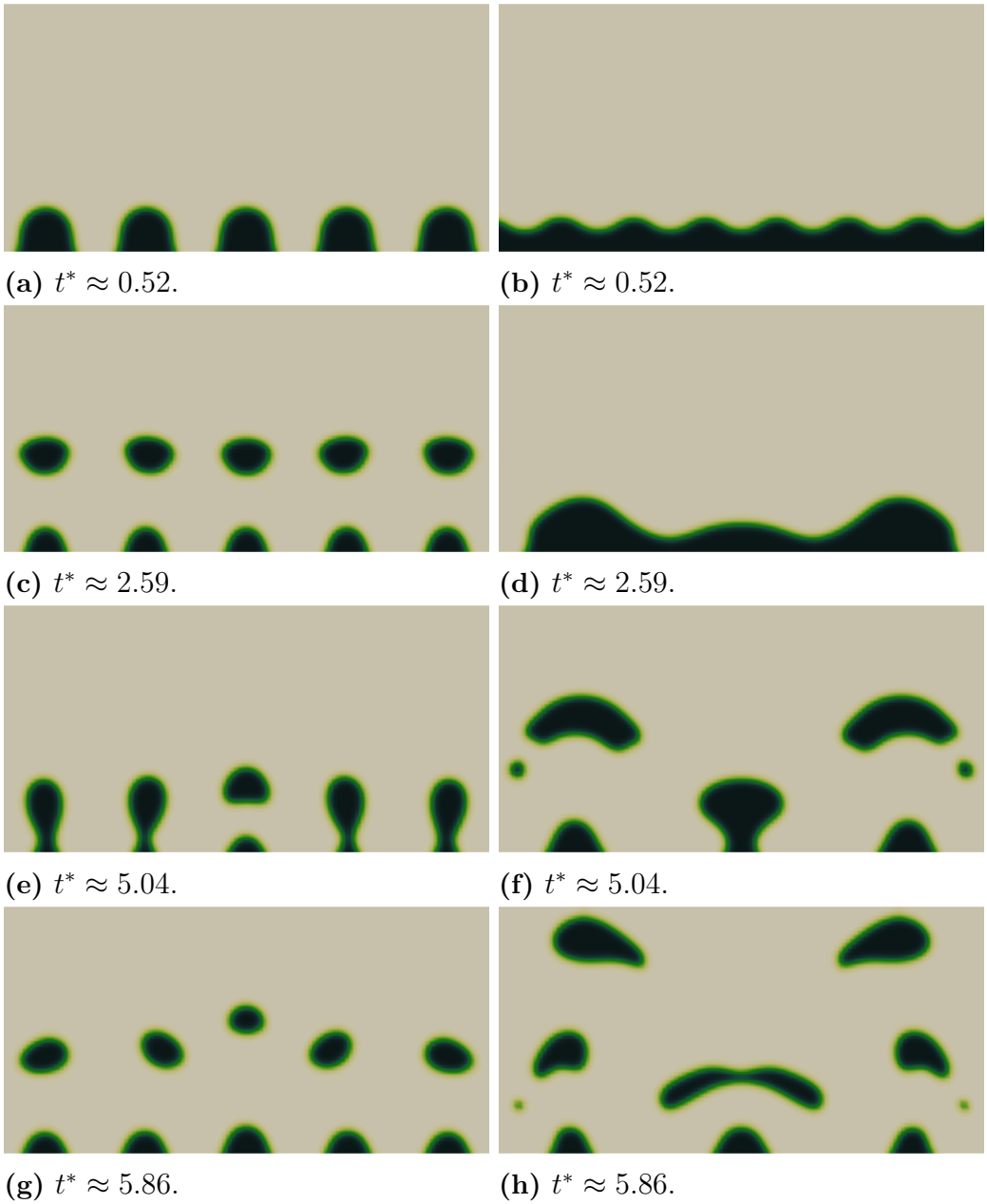

(a) $t^* \approx 0.52$. **(b)** $t^* \approx 0.52$.

(c) $t^* \approx 2.59$. **(d)** $t^* \approx 2.59$.

(e) $t^* \approx 5.04$. **(f)** $t^* \approx 5.04$.

(g) $t^* \approx 5.86$. **(h)** $t^* \approx 5.86$.

Figure 4.7: Volume fraction of vapour for $\Delta = 15\,\mathrm{K}$ and $\theta_w = 120°$ at times $t^* \approx 0.05 - 0.25 - 0.50 - 0.59$. Subfigures $(a) - (c) - (e) - (g)$ report the results for $N_{bub} = 5$ and $(b) - (d) - (f) - (h)$ the results for $N_{bub} = 7$.

In figure 4.7a and 4.7b it is clearly seen that for five nucleation sites the bubbles are separated whereas for seven nucleation sites a film forms. It is observable in figure 4.7d that this film contracts after a few initial oscillations, $t^* \approx 2.59$, due to the effect of surface tension, where three distinct peaks are seen. These peaks are thereafter completely contracted to three distinct bubbles which are later detaching, see figure 4.7f. Note how the the two outer bubbles detach faster than the centre bubble, and that two smaller bubbles are ejected from the larger rising bubbles. In figure 4.7h it can be seen how the first detaching bubbles effect the second wave of bubbles, where the central bubble is separated to the sides due to horizontal forces from the wake of the outer forces. Looking at the setup with 5 nucleation sites it can be seen that a separation of the bubbles are maintained throughout the whole simulation, Subfigures 4.7c, 4.7e and 4.7g. Interesting to see is that the first set of detaching bubbles are almost symmetrical with weak coupling between the bubbles in a sideways direction. However as can be seen at $t^* \approx 5.04$, the central bubbles detaches more quickly for the second departure. This can be further seen at $t^* \approx 5.86$ where the central bubble has a higher vertical position, and also a smaller volume compared to the outer four bubbles. The outer four bubbles are also seen to have obtained some rotation since their shape is rotated with regards to the vertical axis. Inwards rotation for the two inner bubbles and outwards for the two outer.

Figure 4.8 represents the evolution of the non-dimensional heat flux for different number of nucleation cites. Dash-dotted blue line represents $N_{bub} = 1$, black dashed line $N_{bub} = 3$, red long-dashed line $N_{bub} = 5$ and purple dot-dot-dashed line $N_{bub} = 7$.

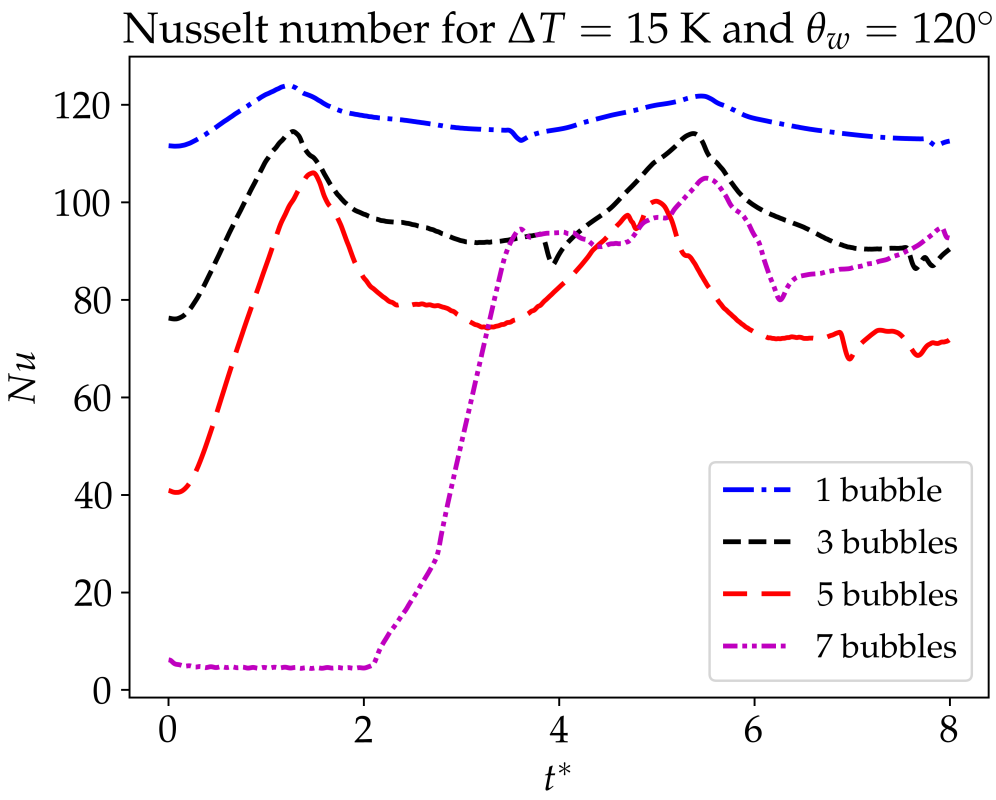

Figure 4.8: Nusselt number $Nu = ql_y/(\kappa_2 \Delta T)$ as function of dimensionless time $t^* = t/\sqrt{l_y/|g|}$ with number of initial bubbles as parameter.

We observe that in general, the total heat flux depends on two mechanisms. As the first mechanicsm, heat conduction decreased as the more surface area of the wall is covered by vapour phase with lower conductivity. On the other hand, as the bubble grows due to phase change, latent heat contributes to the total amount of energy extracted from the wall.

Irrespective of the number of nucleation sites, the heat flux first increases due to higher heat conduction and reaches the maximum value where the first bubble departs. There the remaining bubbles spread out on the surface and heat transfer reduces. This continues until the second nucleus grows large enough to start contracting and the heat flux increases again. This periodic scenario goes on.

Among different cases, for the parameter setup of this study, the surface with a single nucleation cite provides better heat transfer. This can be understood by considering the two abovementioned mechanisms. Having single nucleation cite, smaller portion of the wall is insulated by the film of the vapour, thus higher conduction heat flux is obtained. Even though the phase change heat transfer increases as more bubbles are formed and grown on the wall. However, since the bubble is so large, it departs the wall very soon. As a result, there is not enough time for phase change heat transfer to overcome the conduction.

On the other hand, for the case with 7 nucleation cites, due to rapid formation of the insulating film, initially almost all the wall surface area is insulated by vapour resulting in very small value for heat flux. However, soon after the bubbles merge, due to surface tension forces, the film of vapour forms a large bubble which is subjected to boiling. Thus, there is a rapid and abrupt increase in the heat flux due to phase change over a large bubble. The heat flux increases until the bubble starts departing the wall leaving three nucleation cites behind for the next round of phase change. After this instance, the overal heat flux of the system with 7 initial nucleation cites is very similar to the one with 3 nucleation cites (see the overlap between the black and the purple lines in figure 4.8).

4.5 Heat map

To summarise the results two heat maps of the time averaged Nusselt number $\overline{Nu}$ will be presented. It is calculated as:

$$\overline{Nu} = \frac{\int_0^{T_f} Nu dt}{\int_0^{T_f} dt} \tag{4.5}$$

where $T_f = 3t_{ff}$. Here more simulations are included then were presented in the figures in the last chapters. Simulations were performed for $\theta_w = [45°, 60°, 90°, 120°]$, $\Delta T = [2.5\,\mathrm{K}, 5\,\mathrm{K}, 7.5\,\mathrm{K}, 10\,\mathrm{K}, 12.5\,\mathrm{K}, 15\,\mathrm{K}]$ and $N_{bub} = [1, 2, 3, 4, 5, 6]$. The first heat map represents superheat temperature ΔT on the x-axis and contact angle θ_w on the y-axis for one nucleation site and is show in Figure 4.9.

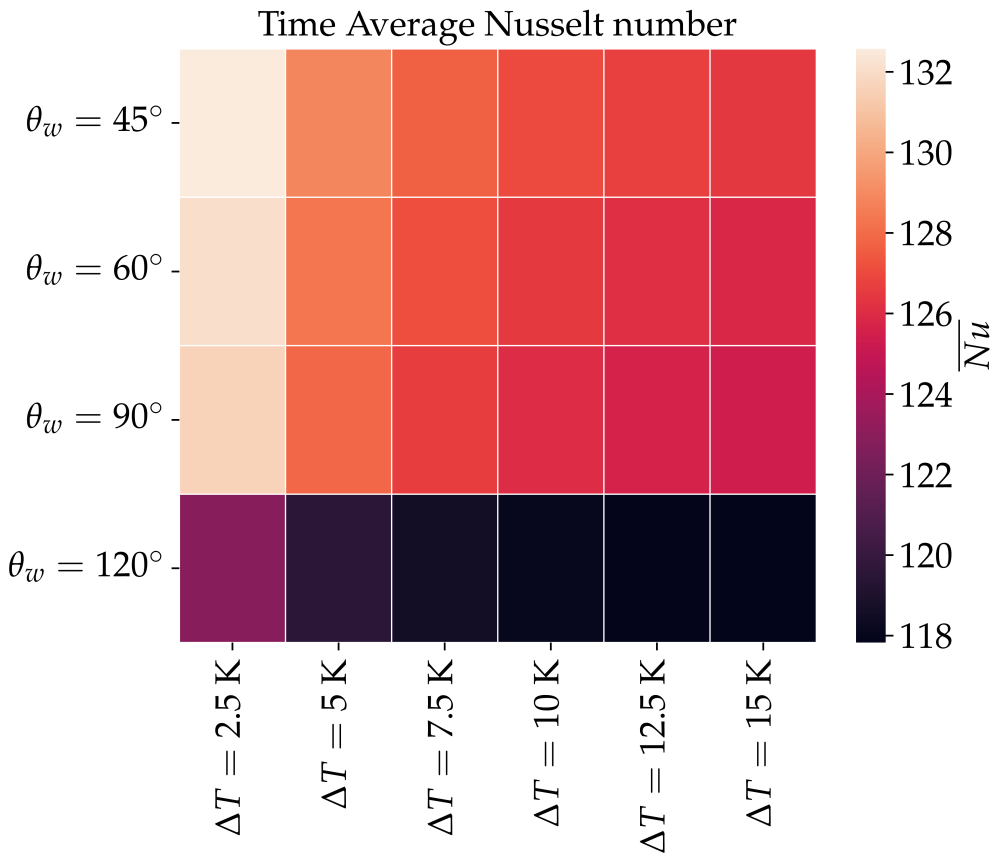

Figure 4.9: Heat map of the time averaged Nusselt number as a function of superheat temperature $\Delta T = [2.5\,\mathrm{K}, 5\,\mathrm{K}, 7.5\,\mathrm{K}, 10\,\mathrm{K}, 12.5\,\mathrm{K}, 15\,\mathrm{K}]$ and static contact angle $\theta_w = [45°, 60°, 90°, 120°]$.

Highest average Nusselt number is found for the lowest superheat temperature $\Delta T = 2.5\,\mathrm{K}$ and the most hydrophilic contact angle $\theta_w = 45°$. This can be understood by quickest departure time for hydrophilic angles, most liquid-wall contact and largest ratio of latent heat transfer to conduction heat transfer for lowest superheat temperature. Lowest Nusselt number is found for the most hydrophobic contact angle $\theta_w = 120°$ and superheat temperature $\Delta T = 15\,\mathrm{K}$.

The parameters of the second heat map are initial bubbles N_{bub} and static contact angle θ_w with fixed superheat temperature $\Delta T = 5\,\mathrm{K}$, and is presented in Figure 4.10.

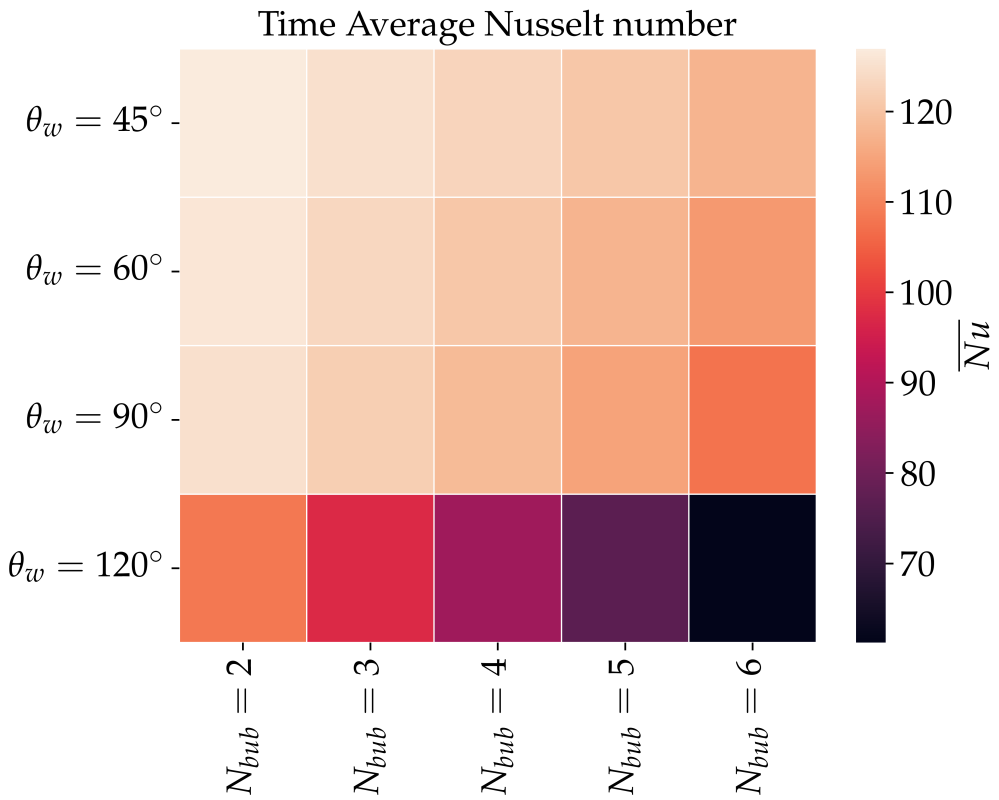

Figure 4.10: Heat map of the time averaged Nusselt number as a function of number of initial bubbles $N_{bub} = [2, 3, 4, 5, 6]$ and static contact angle $\theta_w = [45°, 60°, 90°, 120°]$.

The general trend is observed that the average Nusselt number decreases for higher number of nucleation sites. This trend is most prominent for $\theta_w = 120°$ due to the slower bubble detachment and longer contact time between bubble and wall. This longer contact time enhances the effect of the number of initial bubbles compared to the hydrophilic contact angles with faster departure and shorter contact times.

4.6 Discussion

Based on the Nusselt number results from Figures 4.9 and 4.10 the maximum heat flux is found for $\theta_w = 45°$, $\Delta T = 2.5\,\mathrm{K}$ and $N_{bub} = 1$. This is the configuration that allows for the maximum contact area between liquid and wall for the largest amount of time. To understand this we can note that the liquid water has 24 times larger heat conduction coefficient than the steam, allowing for faster conduction of the heat from the wall. This result seems to indicate that the heat flux is dominated by heat conduction of the liquid water compared to phase change. The results from Figure 4.6 further confirm this observation since the heat flux is higher without any phase change, after the departure of the hydrophilic bubbles, compared to the hydrophobic bubble, where phase change is present.

The cause of this disagreement with literature, that phase change increases heat flux, can be manifolded. Firstly the gravitational effects on the departure of the bubble were nonphysically large compared to surface tension and thermal effects since our simulated bubble had the diameter 1 cm, approximately one order of magnitude larger than typical bubble sizes of departure in nucleate boiling. That means that the simulated bubbles were initially already larger than the critical departure size, detaching from the surface even without any growth. The growth phase of the bubble, from nucleus to departure size, is therefore not simulated and the majority of the phase change is not taken into account. In effect this means that the increase in heat transfer that occurs for nucleate boiling due to bubble nucleation is missed. However the algorithm became unstable when systems with smaller Eötvös number, i.e. larger surface tension compared to gravity, were simulated. If smaller bubbles could have been simulated, a smaller initiation nucleus could have been used, capturing the growth phase of the bubble as well and possibly seeing larger phase change effects.

Secondly, another source of the unexpected results could be due to the relatively low grid resolution used in the simulations. However unstable behaviour was noted for finer grid, which greatly restricted the mesh resolutions that could be used. Lastly the problem could arise from the phase change implementation itself, but more investigation into the matter is needed.

This unstable behaviour shown by the algorithm severely limited the setups that could be used for the simulations. Therefore not all cases could be explored as desired and the anticipated physical phenomena was not observed as initially expected. The cause for these instabilities are not entirely known, but one surmise is that the level-set function in the interface regularisation faces some problems. The level-set function spreads across the domain and shows oscillatory behaviour after some time after initialisation. Maybe the combination of solving for the phasic masses instead of volume fraction combined with phase change leads to some instabilities.

However one conclusion that can be drawn is that heat conduction is dominating for large bubbles. This indirect indicates that it is in the early stages of bubble growth that the main heat transfer contribution from phase transfer comes from.

5

Conclusion & Outlook

In this chapter the thesis project and the results will be summarised. Based on the discussion from the previous chapter the main outcome of the project will be concluded. Lastly a discussion about future opportunities will be presented.

5.1 Summary & conclusion

In this project we investigated the effect of contact angle, wall superheat temperature and nucleation site density on the wall heat flux and departure of boiling steam bubbles with initial diameters $d_0 = 1\,\text{cm}$ in quiescent liquid water. To investigate this problem a numerical approach has been used, using a novel DI-algorithm for weakly compressible flow. The Nusselt number based on the heat flux through the wall was calculated over time and compared for different sets of parameters. Maximum Nusselt number was found for $\Delta T = 2.5\,\text{K}$, $\theta_w = 45°$ and $N_{bub} = 1$, which were the lowest values for superheat temperature, contact angle and number of nucleation sites in the performed simulations. This indicates that maximum liquid-wall contact is desirable for maximum heat transfer due to the high heat conduction of liquid water compared to steam. The effect of heat transfer due to phase change was found negligible compared to conductive heat transfer.

The results are not in agreement with theory and experiments of nucleate boiling since the simulated bubbles had initial diameters of $d_0 = 1\,\text{cm}$, several orders of magnitude larger than physical nuclei. This initial bubble size is larger than the critical departure size leading to instant detachment. That means that the nucleus growth where most of the phase change occurs was not simulated, thus failing to capture the latent heat transfer of nucleate boiling correctly. Smaller bubbles were not simulated due to instabilities in the simulation code, restricting the lower bubble size. Further improvements of the method has to be done before the algorithm is suitable for simulation of nucleate boiling.

5.2 Future opportunities

Firstly the algorithm need to be improved, such that it is stable for bubbles of physical size in nucleate boiling. Thereafter numerous interesting phase change

phenomena could be investigated.

This project investigated only the short term behaviour of nucleate boiling, looking at one bubble departure for hydrophilic cases and two in hydrophobic cases. To investigate the long term behaviour a nucleation implementation has to be added for the hydrophilic angles when no vapour is left at the wall and hence no new bubble automatically forms in the model. New insights could probably be drawn from longer simulations and perhaps some new trends regarding the contact angle are to be seen. With this new implementation the code could be coupled to an optimisation algorithm, potentially finding the optimal wall conditions for maximum heat transfer coefficient. Another interesting phenomena that could be investigated is a biphilic surface, i.e. surface with hydrophilic and hydrophobic regions. Bubble behaviour will be different and pinning at the transition from hydrophobic to hydrophilic will be observed with potential effect on heat flux. As a last suggestion flow boiling can be investigated, forcing the fluid to flow over the surface. Flow boiling has many important applications within heat management since the fluid often is flowing above the surface.

Bibliography

1. Attinger, D. *et al.* Surface engineering for phase change heat transfer: A review. *MRS Energy amp; Sustainability* **1,** E4 (2014).
2. Balaji, C., Balaji, S. & Gedupudi, S. in *Heat Transfer Engineering* (eds Balaji, C., Balaji, S. & Gedupudi, S.) 351–396 (Academic Press, 2021). ISBN: 978-0-12-818503-2. https://www.sciencedirect.com/science/article/pii/B9780128185032000113.
3. Crowe, C. *Multiphase Flow Handbook* ISBN: 9781420040470. https://books.google.se/books?id=7FDbB7VjxkQC (CRC Press, 2005).
4. Shahmardi, A. *Numerical study of interface dynamics and phase change* QC 221026. PhD thesis (KTH, Engineering Mechanics, 2022), 81. ISBN: 978-91-8040-393-1.
5. Brennen, C. & Brennen, C. *Fundamentals of Multiphase Flow* ISBN: 9780521848046. https://books.google.se/books?id=F7hEfx2GUPYC (Cambridge University Press, 2005).
6. Melka, B. *et al.* Multiphase simulation of blood flow within main thoracic arteries of 8-year-old child with coarctation of the aorta. *Heat and Mass Transfer* **54,** 2405–2413. https://doi.org/10.1007/s00231-017-2136-y (2018).
7. Faghri, A. & Zhang, Y. in *Transport Phenomena in Multiphase Systems* (eds Faghri, A. & Zhang, Y.) 765–852 (Academic Press, Boston, 2006). ISBN: 978-0-12-370610-2. https://www.sciencedirect.com/science/article/pii/B9780123706102500155.
8. Van Ouwerkerk, H. Burnout in pool boiling the stability of boiling mechanisms. *International Journal of Heat and Mass Transfer* **15,** 25–34. ISSN: 0017-9310. https://www.sciencedirect.com/science/article/pii/0017931072901639 (1972).
9. Yu, L.-H., Xu, S.-X., Ma, G.-Y. & Wang, J. Experimental Research on Water Boiling Heat Transfer on Horizontal Copper Rod Surface at Sub-Atmospheric Pressure. *Energies* **8,** 10141–10152 (Sept. 2015).
10. Liao, L., Bao, R. & Liu, Z.-H. Compositive effects of orientation and contact angle on critical heat flux in pool boiling of water. *Heat and Mass Transfer* **44,** 1447–1453 (Oct. 2008).
11. Rahman, M., Pollack, J. & McCarthy, M. Increasing Boiling Heat Transfer using Low Conductivity Materials. *Scientific Reports* **5,** 13145 (Aug. 2015).
12. Scapin, N. *et al. Contact-line treatment for phase-changing flows in a diffuse interface framework* QC 20221122.

13. Townsend, R. M. & Rice, S. A. Molecular dynamics studies of the liquid–vapor interface of water. *The Journal of Chemical Physics* **94,** 2207–2218. ISSN: 0021-9606. eprint: https://pubs.aip.org/aip/jcp/article-pdf/94/3/2207/11057020/2207_1_online.pdf. https://doi.org/10.1063/1.459891 (Feb. 1991).
14. Chen, S. & Doolen, G. D. LATTICE BOLTZMANN METHOD FOR FLUID FLOWS. *Annual Review of Fluid Mechanics* **30,** 329–364. eprint: https://doi.org/10.1146/annurev.fluid.30.1.329. https://doi.org/10.1146/annurev.fluid.30.1.329 (1998).
15. Colombo, M. & Fairweather, M. in *26th European Symposium on Computer Aided Process Engineering* (eds Kravanja, Z. & Bogataj, M.) 445–450 (Elsevier, 2016). https://www.sciencedirect.com/science/article/pii/B9780444634283500795.
16. Trujillo, M. F. Reexamining the one-fluid formulation for two-phase flows. *International Journal of Multiphase Flow* **141,** 103672. ISSN: 0301-9322. https://www.sciencedirect.com/science/article/pii/S0301932221001208 (2021).
17. Mirjalili, B. S., Jain, S. S. L. & Dodd, M. S. *Interface-capturing methods for two-phase flows : An overview and recent developments* in (2017).
18. Peskin, C. S. The immersed boundary method. *Acta Numerica* **11,** 479–517 (2002).
19. Tryggvason, G. *et al.* A Front-Tracking Method for the Computations of Multiphase Flow. *Journal of Computational Physics* **169,** 708–759. ISSN: 0021-9991. https://www.sciencedirect.com/science/article/pii/S0021999101967269 (2001).
20. Hirt, C. & Nichols, B. Volume of fluid (VOF) method for the dynamics of free boundaries. *Journal of Computational Physics* **39,** 201–225. ISSN: 0021-9991. https://www.sciencedirect.com/science/article/pii/0021999181901455 (1981).
21. Dervieux, A. & Thomasset, F. *A finite element method for the simulation of a Rayleigh-Taylor instability* in (1980).
22. Demou, A. D., Scapin, N., Pelanti, M. & Brandt, L. A pressure-based diffuse interface method for low-Mach multiphase flows with mass transfer. *Journal of Computational Physics* **448,** 110730. ISSN: 0021-9991. https://www.sciencedirect.com/science/article/pii/S0021999121006252 (2022).
23. Baer, M. & Nunziato, J. A two-phase mixture theory for the deflagration-to-detonation transition (ddt) in reactive granular materials. *International Journal of Multiphase Flow* **12,** 861–889. ISSN: 0301-9322. https://www.sciencedirect.com/science/article/pii/0301932286900339 (1986).
24. Abgrall, R. How to Prevent Pressure Oscillations in Multicomponent Flow Calculations: A Quasi Conservative Approach. *Journal of Computational Physics* **125,** 150–160. ISSN: 0021-9991. https://www.sciencedirect.com/science/article/pii/S0021999196900856 (1996).
25. Brackbill, J., Kothe, D. & Zemach, C. A continuum method for modeling surface tension. *Journal of Computational Physics* **100,** 335–354. ISSN: 0021-9991.

https://www.sciencedirect.com/science/article/pii/002199919290240Y (1992).

26. Le Métayer, O. & Saurel, R. The Noble-Abel Stiffened-Gas equation of state. *Physics of Fluids* **28,** 046102. eprint: https://doi.org/10.1063/1.4945981. https://doi.org/10.1063/1.4945981 (2016).
27. Jain, S. Accurate conservative phase-field method for simulation of two-phase flows (Mar. 2022).
28. Shahmardi, A., Rosti, M., Tammisola, O. & Brandt, L. A fully Eulerian hybrid immersed boundary-phase field model for contact line dynamics on complex geometries. *Journal of Computational Physics* **443,** 110468 (May 2021).
29. Huang, Z., Lin, G. & Ardekani, A. Implementing contact angle boundary conditions for second-order Phase-Field models of wall-bounded multiphase flows (Mar. 2021).
30. Amsden, A. A. & Harlow, F. H. A simplified MAC technique for incompressible fluid flow calculations. *Journal of Computational Physics* **6,** 322–325. ISSN: 0021-9991. https://www.sciencedirect.com/science/article/pii/002199917090029X (1970).
31. Falgout, R. D. & Yang, U. M. *hypre: A Library of High Performance Preconditioners* in *Computational Science — ICCS 2002* (eds Sloot, P. M. A., Hoekstra, A. G., Tan, C. J. K. & Dongarra, J. J.) (Springer Berlin Heidelberg, Berlin, Heidelberg, 2002), 632–641. ISBN: 978-3-540-47789-1.
32. Pelanti, M. Arbitrary-rate relaxation techniques for the numerical modeling of compressible two-phase flows with heat and mass transfer. *International Journal of Multiphase Flow* **153,** 104097 (Apr. 2022).
33. Kang, M., Fedkiw, R. P. & Liu, X.-D. A Boundary Condition Capturing Method for Multiphase Incompressible Flow. *Journal of Scientific Computing* **15,** 323–360. https://doi.org/10.1023/A:1011178417620 (2000).

DEPARTMENT OF MECHANICS AND MARITIME SCIENCES
CHALMERS UNIVERSITY OF TECHNOLOGY
Gothenburg, Sweden
www.chalmers.se

CHALMERS
UNIVERSITY OF TECHNOLOGY